A non-axisymmetric potential for the Milky Way disk

Y. R. Khalil[1] ⋆, B. Famaey[1], G. Monari[1], M. Bernet[2,3,4], A. Siebert[1], R. Ibata[1], G. F. Thomas[5,6],
P. Ramos[7], T. Antoja[2,3,4], C. Li[8,9], S. Rozier[10], and M. Romero-Gómez[2,3,4]

1 Université de Strasbourg, CNRS UMR 7550, Observatoire astronomique de Strasbourg, 11 rue de l'Université, 67000 Strasbourg, France
2 Departament de Física Quàntica i Astrofísica (FQA), Universitat de Barcelona (UB), C Martí i Franquès, 1, 08028 Barcelona, Spain
3 Institut de Ciències del Cosmos (ICCUB), Universitat de Barcelona (UB), C Martí i Franquès, 1, 08028 Barcelona, Spain
4 Institut d'Estudis Espacials de Catalunya (IEEC), Edifici RDIT, Campus UPC, 08860 Castelldefels, Barcelona, Spain
5 Instituto de Astrofísica de Canarias, E-38205 La Laguna, Tenerife, Spain
6 Universidad de La Laguna, Dpto. Astrofísica, E-38206 La Laguna, Tenerife, Spain
7 National Astronomical Observatory of Japan, Mitaka-shi, Tokyo 181-8588, Japan
8 School of Astronomy and Space Science, Nanjing University, Nanjing 210093, People's Republic of China
9 Key Laboratory of Modern Astronomy and Astrophysics (Nanjing University), Ministry of Education, Nanjing 210093, People's Republic of China
10 School of Mathematics and Maxwell Institute for Mathematical Sciences, University of Edinburgh, Kings Buildings, Edinburgh, EH9 3FD, UK

ABSTRACT

We provide a purely dynamical global map of the non-axisymmetric structure of the Milky Way disk. For this, we exploit the information contained within the in-plane motions of disk stars from Gaia DR3 to adjust a model of the Galactic potential, including a detailed parametric form for the bar and spiral arms. We explore the parameter space of the non-axisymmetric components with the backward integration method, first adjusting the bar model to selected peaks of the stellar velocity distribution in the Solar neighbourhood, and then adjusting the amplitude, phase, pitch angle and pattern speed of spiral arms to the median radial velocity as a function of position within the disk. We check a posteriori that our solution also qualitatively reproduces various other features of the global non-axisymmetric phase-space distribution, including most of the moving groups and phase-space ridges despite those not being primarily used in the adjustment. This fiducial model has a bar with pattern speed 37 km s^{-1} kpc^{-1} and two spiral modes that are two-armed and three-armed respectively. The two-armed spiral mode has a ∼ 25 % local contrast surface density, a low pattern speed of 13.1 kms^{-1}kpc^{-1}, and matches the location of the Crux-Scutum, Local and Outer arm segments. The three-armed spiral mode has a ∼ 9 % local contrast density, a slightly higher pattern speed of 16.4 kms^{-1}kpc^{-1}, and matches the location of the Carina-Sagittarius and Perseus arm segments. The Galactic bar, with a higher pattern speed than both spiral modes, has recently disconnected from those two arms. The fiducial non-axisymmetric potential presented in this paper, reproducing most non-axisymmetric signatures detected in the stellar kinematics of the Milky Way disk, can henceforth be used to confidently integrate orbits within the Galactic plane.

Key words. Galaxy: general – Galaxy: kinematics and dynamics – Galaxy: structure – Galaxy: evolution – Galaxy: disk

1. Introduction

The Gaia mission now provides full six-dimensional phase-space information on the Milky Way (MW) disk for a larger number of stars, and over a larger volume, than ever before. The second (Gaia Collaboration et al. 2018a), early-third (Gaia Collaboration et al. 2021), and third (DR3, Gaia Collaboration et al. 2023a) data releases of Gaia have represented important milestones in this regard. Whilst stellar vertical motions have revealed in recent years a disequilibrium of the Galactic disk (Antoja et al. 2018), possibly related to a subtle interplay between external perturbations and internal non-axisymmetries (e.g., Binney & Schönrich 2018; Laporte et al. 2019; Li et al. 2023; Tremaine et al. 2023; Frankel et al. 2024), the rich information contained solely within the in-plane motions of stars (e.g., Gaia Collaboration et al. 2018b, 2023b) has not been fully exploited yet. Indeed, these in-plane motions should – in principle – allow us to get a detailed dynamical mapping of the most important

non-axisymmetric structures of the MW disk, namely the Galactic bar and the spiral arms (Lynden-Bell & Kalnajs 1972). However, such a detailed mapping is still lacking. This is the focus of the present study.

The existence of the MW bar was originally hypothesized from the observations of gas kinematics (de Vaucouleurs 1964; Peters 1975; Gerhard & Vietri 1986; Binney et al. 1991) and confirmed from near-infrared observations (e.g., Sellwood 1993; Weiland et al. 1994; Binney et al. 1997) as well as bulge stellar kinematics (e.g., Zhao et al. 1994). It is nowadays clear that a large fraction of stars in the bulge region indeed follow a rotating, barred, boxy/peanut-shaped structure connected to an edge-on bar, whose pattern speed, $\Omega_{\rm b}$, is nevertheless still subject to debate. Less than three decades ago, a consensus emerged for a pattern speed in the range $\Omega_{\rm b}$ ~ 50 km s^{-1} kpc^{-1} – 60 km s^{-1} kpc^{-1} from various lines of evidence, such as hydrodynamical simulations comparing the modeled gas flow to observed Galactic CO and HI longitude-velocity diagrams (Fux 1999; Englmaier & Gerhard 1999; Bissantz et al. 2003), the

⋆ e-mail: yassin.khalil@unistra.fr

Tremaine & Weinberg (1984) method applied to stars in the inner Galaxy (Debattista et al. 2002), or local stellar kinematics (Dehnen 1999b, 2000; Fux 2001) positioning the Sun marginally beyond the 2:1 Outer Lindblad Resonance (OLR) of the bar. The latter argument has been supported by numerous subsequent analyses (e.g. Minchev et al. 2007; Quillen et al. 2011; Antoja et al. 2012, 2014; Fragkoudi et al. 2019), while on the contrary, parallel research on the density of red clump stars in the disk (Wegg et al. 2015), gas kinematics (Sormani et al. 2015; Li et al. 2016), dynamical modeling of stellar kinematics in the inner Galaxy (Portail et al. 2017), and proper motion data from the VVV survey (e.g., Clarke et al. 2019), including with the Tremaine-Weinberg method (Sanders et al. 2019), have collectively pointed to a revised pattern speed of $\Omega_b \sim 35$ km s^{-1} kpc^{-1} $- 40$ km s^{-1} kpc^{-1}. Pérez-Villegas et al. (2017) and Monari et al. (2019b) subsequently demonstrated that the Galactic model adjusted to bulge stellar kinematics by Portail et al. (2017) could effectively replicate several observed features in local velocity space (see also Monari et al. 2019a; Binney 2020; D'Onghia & Aguerri 2020; Lucchini et al. 2024). Such a lower bar pattern speed is also consistent with observed overdensities in the stellar halo phase-space (Dillamore et al. 2024) and with the chemistry of the disk (Haywood et al. 2024). Other intermediate pattern speeds have also been proposed (Hunt & Bovy 2018), and even much lower ones (Horta et al. 2024), while several studies have concluded that stellar kinematics of the disk alone were not sufficient to break the degeneracy (Trick et al. 2021; Trick 2022; Bernet et al. 2024). However, kinematics of stars in the bar region itself seem to have converged to $\Omega_b \sim 35$ km s^{-1} kpc^{-1} $- 40$ km s^{-1} kpc^{-1}, although possible sudden variations of the pattern speed are also possible (Hilmi et al. 2020). Finally, a steady decrease of the pattern speed of the bar with time has been tentatively detected (Chiba et al. 2021; Chiba & Schönrich 2021), and could explain some aspects of the vertical disequilibrium of the Galactic disk (Li et al. 2023), and can partially contribute in explaining the presence of metal-poor stars with prograde planar orbits in the Solar vicinity (Li et al. 2024; Yuan et al. 2024).

Concerning the location and dynamics of spiral arms of the MW, the present observational situation is even less clear than for the bar. The suggestion that the MW could host spiral arms is certainly as old as the realisation that it belongs to the realm of disk galaxies, but due to extinction, it was not before the work of Morgan et al. (1952) that these arms were identified based on the distribution of HII regions, soon followed by the kinematic analysis of the HI 21-cm line by Oort et al. (1958). Based on the distances to OB associations and HII regions, Georgelin & Georgelin (1976) mapped a four-armed spiral pattern, which has been repeatedly confirmed with young or gaseous tracers (e.g. Urquhart et al. 2014), but not with older/redder ones that should better trace the perturbations in the Galactic potential. Indeed, Drimmel (2000), Drimmel & Spergel (2001), Benjamin et al. (2005) and Churchwell et al. (2009) found with near-infrared and mid-infrared tracers that the MW seemingly hosts two main spiral arms. Collecting data on HII regions and giant molecular clouds, Hou et al. (2009) showed that models of three-armed and four-armed logarithmic spirals could connect those different spiral tracers, as reviewed in Shen & Zheng (2020). In summary, it is no exaggeration to say that different tracers and observations are far from converging on parameters describing the positions of each spiral arm segment in the MW disk. The so-called Local arm, for example, has been found by Gaia Collaboration et al. (2023b) and Poggio et al. (2021), tracing young stars, to be more extended – and to have an intermediary pitch angle –

compared to Vázquez et al. (2008) where this arm rather heads outwards to the Perseus arm, or to Xu et al. (2021) where the Local arm heads inwards to the Carina–Sagittarius arm. Similar debates exist regarding the Perseus arm and Outer arm with respect to their position in the disk and pitch angle. Perhaps most strikingly, the pitch angle of the Perseus arm has been found to be $\sim 24°$ in Levine et al. (2006), compatible with results of Poggio et al. (2021), and $\sim 9°$ in Reid et al. (2019), meaning that the name does not actually always refer to the same observed overdensities in the Galactic plane. The situation regarding the pattern speed of spiral arms is even more confused, as its signature can also depend on their dynamical nature and origin (see Sellwood & Masters 2022, for a review). Indeed, numerical simulations of galactic disks offer multiple perspectives on this topic, from transient corotating structures winding up and disappearing quickly (e.g., Baba et al. 2013; Hunt et al. 2018, 2019), to multiple modes persisting over a few (or even many) galactic rotations, falsely appearing as very short-lived due to superposition of modes (e.g., Sellwood & Carlberg 2014). In the following, we will remain relatively agnostic on the exact origin and nature of spiral arms, but two important points will guide our modelling procedure. The first point is the current consensus that, when spirals appear as modes in simulations, these are not strictly static as in the classical density wave picture (Lin & Shu 1964), but are rather made of a recurrent cycle of groove modes (seeded by a depletion of circular orbits in a narrow range of angular momenta, see, e.g. De Rijcke & Voulis 2016; De Rijcke et al. 2019) that live between their inner Lindblad resonance (ILR) and OLR, where they can create new grooves which set up the recurrent cycle (Sellwood & Carlberg 2014, 2019). They can also be edge modes (Fiteni et al. 2024). The amplitudes of the individual modes grow and decay, but they are nevertheless genuine standing wave oscillations with fixed shape and pattern speed, detectable over a period of at least one rotation. The second point is that spectrograms of *N*-body simulations displaying joint bar and spiral perturbations tend to display spiral arms rotating more slowly than the bar; moreover spiral arms are never present within the corotation radius of the bar. These spirals live between their own ILR and OLR but are usually strongest between their ILR and corotation (Quillen et al. 2011).

Keeping all the aforementioned caveats in mind, several tentative measurements of the amplitude and pattern speed of spiral arms have been made over time. Originally, Lin et al. (1969) proposed a 2-armed model with pitch angle of 6° and pattern speed of $\Omega_{s,2} \sim 13$ km s^{-1} kpc^{-1} based on the systematic motion of gas and the displacement of moderately young stars in their classical density wave model. A more recent estimate based on the classical Lin & Shu (1964) density wave formalism has been made by Siebert et al. (2012) fitting the mean radial velocity map from the RAVE survey and finding a best-fit 2-armed spiral model with a contrast surface density of 14%, a pitch angle of 10° and a pattern speed of $\Omega_{s,2} \sim 18.6$ km s^{-1} kpc^{-1}. This model however neglected the effect of the bar (see, e.g. Monari et al. 2014). On the other hand, Amaral & Lepine (1997) argued for a superposition of a 2-armed and 4-armed spiral, both with a pattern speed of ~ 20 km s^{-1} kpc^{-1} based on tracing back open clusters to their birth place. Such a procedure was recently carried out by Castro-Ginard et al. (2021), finding a declining pattern speed with radius from ~ 50 km s^{-1} kpc^{-1} for the Scutum arm segment to ~ 17 km s^{-1} kpc^{-1} for the Perseus arm segment. Modeling the gas flow in the inner Galaxy, Bissantz et al. (2003) obtained a joint measurement of the bar and 4-armed spiral pattern speeds, with a very high pattern speed for the bar, $\Omega_b \sim 60$ km s^{-1} kpc^{-1}, and a 4-armed spiral pattern speed of $\Omega_{s,4} \sim 20$ km s^{-1} kpc^{-1}.

More recently Eilers et al. (2020) applied a toy model of a logarithmic spiral to Gaia DR2 mean Galactocentric radial velocity field to suggest a contrast surface density of $\sim 10\%$, a pitch angle of $12°$ and a fixed pattern speed of $\Omega_{s,2} = 12$ km s^{-1} kpc^{-1} for a 2-armed spiral corresponding to the Local and Outer arms. Regarding the amplitude, the most recent determination, based on the vertical Jeans equation, has found the Local arm to be the strongest local overdensity, with a contrast density of roughly 20% (Widmark & Naik 2024).

Here, we attempt at fully exploiting the rich information encoded within the in-plane stellar motions in Gaia DR3 (Gaia Collaboration et al. 2023b) to constrain dynamically the non-axisymmetries of the Galaxy. The only previous similar attempt is that from Vislosky et al. (2024), comparing three hydrodynamical simulations of galaxies to the velocity maps from Gaia in order to get insights on the bar-spiral orientation. Our approach hereafter is complementary since, instead of qualitatively comparing a self-consistent hydrodynamical simulation to the data, we attempt a more quantitative fit to the stellar phase-space data from Gaia. For this, we will resort to backward integrations to model the velocity field with a parametric form of the gravitational potential. Our preferred solution could then serve as new fiducial non-axisymmetric parametric potential for the Milky Way disk.

In Section 2, we briefly present the data extracted from the RVS sample of Gaia DR3 that we are using to constrain the potential from the MW disk kinematics. The modelling method and the parametrization of the potential are introduced in Section 3, whilst results are presented in Section 4. A posteriori comparisons with observables to which the model was not fit, as well as some examples of applications of our fiducial potential are given in Section 5, before concluding in Section 6.

2. The Gaia RVS disk sample

Since we are planning to use the in-plane motions of disk stars to constrain the non-axisymmetries of the MW, we select a sample of stars with six-dimensional phase-space information from the Gaia RVS close to the Galactic plane. We use data from Gaia DR3 (Gaia Collaboration et al. 2023a) combined with the StarHorse (Anders et al. 2022) distances, and select 17 414 667 stars within a height of 300 pc from the Galactic plane.

We adopt, for the Sun's position $x_\odot$ and velocity $V_\odot$ in Galactocentric Cartesian coordinates, $x_\odot = (x_\odot, y_\odot, z_\odot) = (8275, 0, 15.29)$ pc and $V_\odot = (V_{x_\odot}, V_{y_\odot}, V_{z_\odot}) = (-9.3, 251.5, 8.59)$ km s^{-1} (Gaia Collaboration et al. 2023b; Portail et al. 2017; Widmark & Monari 2019), respectively. We then transform the data from equatorial coordinates to Galactocentric coordinates with the Astropy library (Astropy Collaboration et al. 2022) to compute the stars' positions in Galactocentric Cartesian coordinates, $x = (x, y, z)$ and their in-plane velocities in Galactocentric Cylindrical coordinates, $V = (V_R, V_\varphi)$, with the Galactocentric radius $R = \sqrt{x^2 + y^2}$ and azimuth $\varphi = \arctan(y/x)$, defined to be zero at the azimuth of the Sun. The stars are selected within $4\,\text{kpc} < x < 12\,\text{kpc}$ and $-4\,\text{kpc} < y < 4\,\text{kpc}$.

On Fig. 1, left panel, we display the local stellar velocity distribution for a bit more than 2 million stars within $|R - R_0| < 300$ pc in our sample, where $R_0 = 8.275$ kpc is the Galactocentric radius of the Sun. On this figure several of the well-known moving groups of the Solar neighbourhood (e.g., Dehnen 1998; Famaey et al. 2005; Antoja et al. 2008; Ramos et al. 2018; Bernet et al. 2022) are immedi-

ately visible. The "Hat" can be seen as the downward concave arch at high V_φ, from $(V_R, V_\varphi) \approx (-100 \text{ kms}^{-1}, 270 \text{ kms}^{-1})$ to $(V_R, V_\varphi) \approx (120 \text{ kms}^{-1}, 260 \text{ kms}^{-1})$; The Sirius moving group (e.g., Famaey et al. 2008) is approximately straight at $V_\varphi \approx 255 \text{ kms}^{-1}$, located between $V_R \approx -50 \text{ kms}^{-1}$ and $V_R \approx 0 \text{ kms}^{-1}$, with a peak at $V_R \approx -15 \text{ kms}^{-1}$; Coma is right below Sirius in azimuthal velocity, around $(V_R, V_\varphi) \approx (0 \text{ kms}^{-1}, 245 \text{ kms}^{-1})$; The Hyades moving group (e.g., Famaey et al. 2007; Pompéia et al. 2011) can be seen as a slightly curved downward arch from the over-density at $(V_R, V_\varphi) \approx (20 \text{ kms}^{-1}, 230 \text{ kms}^{-1})$; The Horn is right next to the Hyades, on the other side in V_R: it appears as an arch going through $(V_R, V_\varphi) \approx (-80 \text{ kms}^{-1}, 200 \text{ kms}^{-1})$; finally, the major Hercules moving group is perceived as a bimodality of the whole velocity-plane, with an under-density, just below the Hyades in azimuthal velocity, separating it from the rest of the distribution. Its bimodality appears clearly, with a second overdensity appearing at low V_φ.

Another way to visualize these arches, which however visually erases the asymmetries in radial velocity, is to plot the distribution of stars in the local axisymmetric action space (e.g. Trick et al. 2019, 2021). Indeed, the Galaxy is to first order an axisymmetric quasi-integrable system, and the action-angle variables (J, θ) are the canonical phase-space variables appropriate for studying and perturbing integrable systems. In these coordinates, the Hamiltonian only depends on the actions J, which are integrals of the motion. Each triplet of actions then fully characterizes an integrable orbit, while the angles indicate where a given star is on that particular orbit. The azimuthal action is simply $J_\varphi = R\,V_\varphi$, whilst the radial action J_R encodes the (Galactocentric) radial excursions of a given orbit. On the middle panel of Fig. 1, the arches in local velocity space are now seen as ridges in local action space, characteristic of resonant features (e.g., Monari et al. 2017; Binney 2020).

These features of local velocity and action space, traced with exquisite precision, have however been known for a long time. The most interesting added value of Gaia data releases has been to expand the volume around the Sun where such dynamical features can be studied (e.g., Ramos et al. 2018; Bernet et al. 2022). In order to adjust the non-axisymmetric components of the Galactic potential in the present work, we will however refrain from using the full phase-space distribution of disk stars, and will rather fit the measure of a central tendency as a function of position in the disk, namely the median Galactocentric radial velocity (Gaia Collaboration et al. 2023b). This map of median radial velocity is displayed on the right panel of Fig. 1 and will be the main observable adjusted in the present work. We will check only a posteriori the qualitative agreement with the full phase-space distribution of stars.

3. Modelling

To build our non-axisymmetric potential we start from an axisymmetric one, and subsequently add a bar and spiral arms, defined by several parameters as described in the following subsections. Within the axisymmetric potential, we use a phase-space distribution function (DF), $f(x, V)$, to describe our tracer population. This 1-particle DF is the probability density function of finding one star at the phase-space point (x, V) and, for a collisionless system, it obeys the collisionless Boltzmann (or Vlasov) equation. Such a DF, for any steady-state integrable stellar system, should solely be a function of isolating integrals of the motion according to the Jeans theorem (Binney & Tremaine 2008).
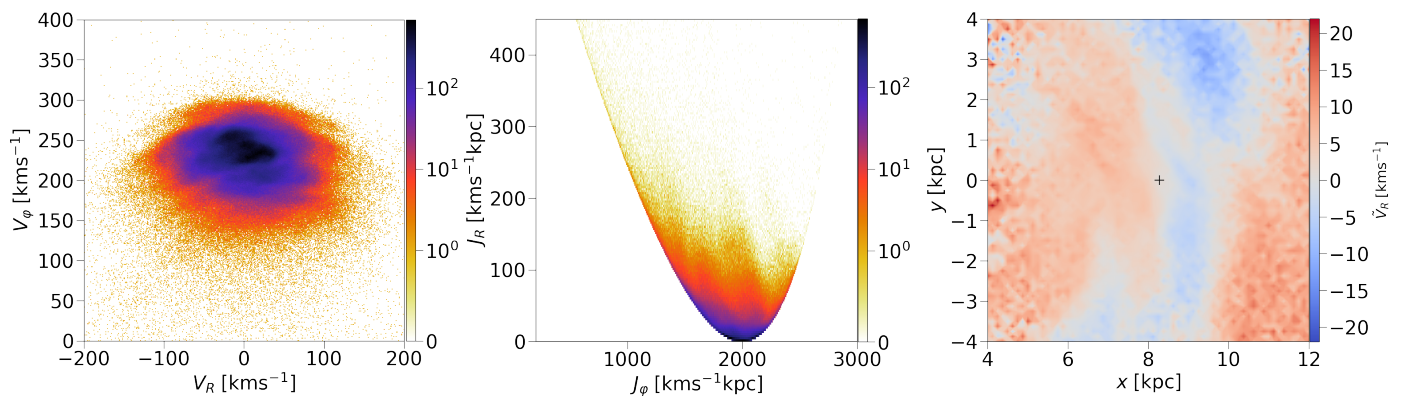
Fig. 1. Left panel: 2-dimensional histogram of the number density of stars from the Gaia RVS disk sample within 300 pc from the Sun on the (V_R, V_φ) plane defined on a $[-200, 200]$ kms^{-1} $\times$ $[0, 400]$ kms^{-1} grid, binned with $(1$ kms$^{-1})^2$ bins. Middle panel: Same distribution on the (J_φ, J_R) plane (computed with `AGAMA` in the potential of Table 1) defined on a $[0, 600]$ kms^{-1} kpc^{-1} $\times$ $[200, 3000]$ kms^{-1} kpc^{-1} grid, binned with $(3 \times 2$ km^2 s^{-2} kpc$^{-2})$ bins. Right panel: the median radial velocity $\tilde{V}_R(x, y)$ as a function of the position in the Galactic plane for the full sample of 17 414 667 stars with $|z| < 300$ pc. The grid is defined as $[4, 12]$ kpc $\times$ $[-4, 4]$ kpc, binned with $(125$ pc$)^2$ bins. The Galactic center is located at $(x, y) = (0$ kpc$, 0$ kpc$)$, the Sun at $(x, y) = (8.275$ kpc$, 0$ kpc$)$ is represented with a cross, and the sense of rotation of the Galaxy is anti-clockwise.
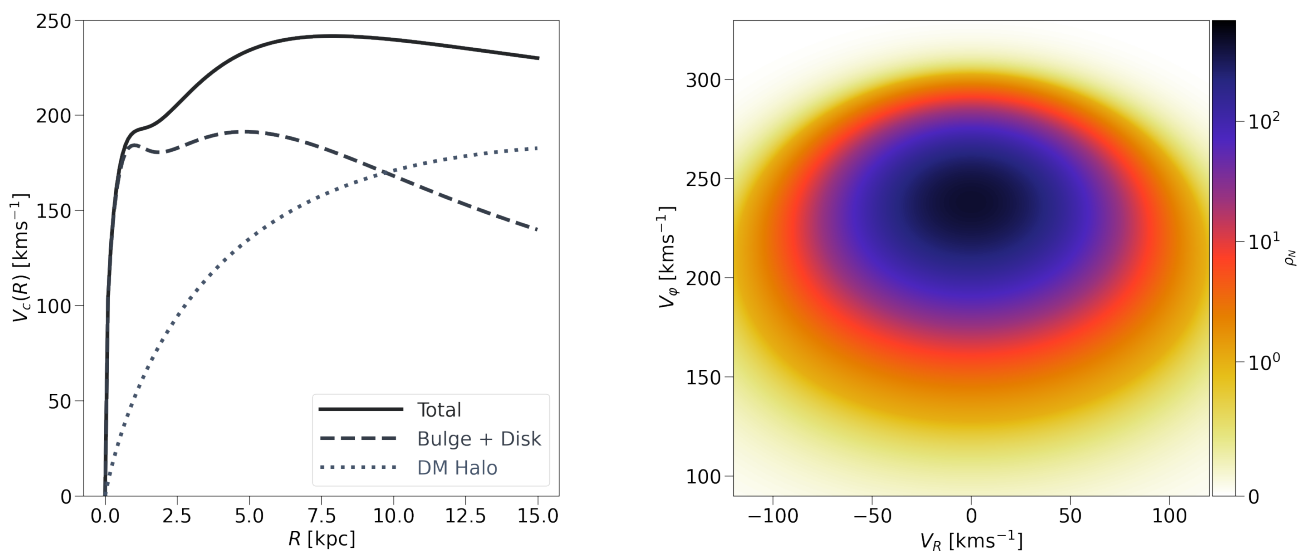

Fig. 2. The axisymmetric background. Left panel: the circular velocity curve of the background axisymmetric potential described in Sec. 3.1. Right panel: The number density ρ_N of stars in velocity space at the Sun's position from the equilibrium DF described in Sec. 3.2, for a normalization factor such that the total number in the model at the Sun is the same as found in the data within 300 pc from the Sun.

We take these integrals to be the actions $\boldsymbol{J}$. In order to transform stellar positions and velocities into actions, one can use an approximation based on Stäckel potentials (see, e.g., Famaey & Dejonghe 2003). Axisymmetric Stäckel potentials are expressed in a spheroidal coordinate system, defined by a focal distance, which is always related to the first and second derivatives of the potential at any given position. Thus, by using the actual Galactic potential at any given position, one can compute an equivalent focal distance as if the potential were locally of Stäckel form, allowing for the calculation of the (quasi-)integrals of the motion and corresponding actions. This "Stäckel fudge" (Binney 2012; Sanders & Binney 2016) is fully implemented within the the Action-based Galaxy Modelling Architecture code (Vasiliev 2018, 2019, `AGAMA`) that we use in the present study.

We are starting from an equilibrium DF, $f(\boldsymbol{J})$, for the tracer population defined within an axisymmetric potential. The first route to include the effect of non-axisymmetric components is to treat them through perturbation theory (e.g. Monari et al. 2016a; Al Kazwini et al. 2022) which, in order to be truly quantitative, needs a special treatment for the resonant zones for a constant pattern speed perturbation (e.g. Monari et al. 2017; Laporte et al. 2020; Binney 2020; Hamilton et al. 2023). This becomes however practically very complicated in the presence of multiple perturbers with different pattern speeds, whose resonances will overlap. To circumvent this issue, one can fortunately rely on the property encoded in the collisionless Boltzmann equation, that the DF value in an infinitesimal Lagrangian volume is conserved. This allows us to use the classical method of backward integration (Vauterin & Dejonghe 1997), used in, e.g., Dehnen (2000); Hunt & Bovy (2018); Hunt et al. (2018, 2019); Monari et al. (2019b); Bernet et al. (2024), in order to explore the shape of the DF.

In order to compute the $f(\boldsymbol{x}, \boldsymbol{V}, t)$, at current time $t = 0$, at the phase-space point $(\boldsymbol{x}, \boldsymbol{V})$, in the presence of the bar and spiral

arms, we backward integrate the orbit for a fixed integration time to its phase-space position $(\boldsymbol{x}', \boldsymbol{V}')$ at time $t' < 0$, before the actual appearance of the non-axisymmetric perturbers. Assuming that the tracer population is represented by the equilibrium DF, $f(\boldsymbol{J})$, in the axisymmetric background potential at time t', we transform $(\boldsymbol{x}', \boldsymbol{V}')$ to action-angle variables using AGAMA, compute the value of the DF[1], and since this value in an infinitesimal Lagrangian volume is conserved, we attribute the same value of the DF to the phase-space position $(\boldsymbol{x}, \boldsymbol{V})$ at present time $t = 0$ in the presence of the bar and spirals. In practice, the orbits are integrated within the plane only, by solving the initial value problem with the Runge-Kutta of order 5 method odeint solver from the very efficient torchdiffeq library (Chen 2018) in PyTorch (Paszke et al. 2019). Doing this at numerous phase-space locations allows us to compute the median radial velocity as a function of position in the disk, and to adjust the parameters of the non-axisymmetric components in order to fit the observed values. In practice the median radial velocity at each grid position (sampled every 50 pc in x and y) on the disk is computed after locally integrating the values of the DF in V_φ for a grid of velocities on which the backward integration is performed at each position. This grid ranges from -79 kms^{-1} to 79 kms^{-1} wit a step of 2 kms^{-1} in V_R, and from 110 kms^{-1} to 330 kms^{-1} with a step of 4 kms^{-1} in V_φ. The potential is evaluated on a grid of radii that is subsequently interpolated with a cubic spline in the torchcubicspline library in Pytorch to improve computational time. Similarly, we also interpolate, with Scipy (Virtanen et al. 2020), a cubic spline to the actions computed with AGAMA.

There are three caveats with the method, which are worth mentioning even though addressing them in detail is far beyond the scope of this first quantitative approach to the problem. First, we are using the full disk sample described in the previous section without taking into account a detailed selection function, assuming that the high number of stars that we use allows for a good estimate of the true median velocity. The second caveat is that, in practice, the observed stellar DF is always measured over finite phase-space volumes whilst the backward integration method operates under the assumption that the mean value of the DF within a given phase-space volume is equivalent to its value at the central point, irrespective of how the volume deforms during the system's orbital evolution. In other words, the backward integration method yields the fine-grained DF, which will typically remain unsmoothed at small scales, whilst the measurable DF within observations is the coarse-grained one, which does *not* obey the collisionless Boltzmann equation (as this coarse-grained DF is smoothed by phase-mixing within finite volumes). In practice, this means that, if the integration is carried out for too long, the fine-grained DF tracked by the backward integration method will lead to sharp and unsmoothed features in velocity space, where chaotic features will also appear as sharper than in the real world. To circumvent this problem, the integration must be carried out only for a relatively limited time, adjusted so that the sharpness of resonant features in velocity space resembles what is observed. Luckily, N-body simulations indicating the existence of recurrent cycles of groove modes in galactic disks (Sellwood & Carlberg 2014, 2019) allow us to consider that current spiral arm modes of the Milky Way are rather recent. This assumption is, of course, not ideal for the bar, but it is

reasonable to assume that the *location* of the resonant features in local velocity space will not evolve with time, whilst their sharpness will. Hence, we will only deal with the location of resonant features in local velocity space to constrain the pattern speed of the bar, and rely on a parametric form of its potential adjusted to the dynamics of the bulge region (Portail et al. 2017; Thomas et al. 2023) for its amplitude. It would be too costly to resort to a forward integration method within the fitting scheme that we set out to apply in the present paper, given the size of the parameter space to explore, and given that each combination of parameters requires a full backward integration of the whole Galactic plane. However, the results obtained hereafter could serve as a basis for forward-in-time test-particle simulations, also expanded to three-dimensions, that we plan to present in a follow-up paper. Finally, a third and last caveat is that our simulations are, by design, not self-consistent. This simplification is much more efficient to explore a vast parameter space. However, future improvements of our method might rely on an adaptation of the made-to-measure method (Syer & Tremaine 1996; Portail et al. 2017) to account for self-consistency, using the results presented hereafter as a basis.

3.1. Background axisymmetric potential

As outlined hereabove, the method uses an axisymmetric background potential. In practice, we assume a 3D axisymmetric density profile and the potential is computed by solving Poisson's equation with AGAMA. The density profile is the summed density of each of the following components: stellar disk, gas disk, bulge and dark matter halo.

The stellar and gas disk density profiles are parametrized in Galactocentric cylindrical coordinates (R, z) as:

$$\rho_{\text{disky}}(R, z) = \frac{\Sigma_0}{2h_z} \exp\left(-\left|\frac{z}{h_z}\right|\right) \exp\left(-\frac{R}{h_R}\right), \quad (1)$$

with the central surface density Σ_0, scale height h_z (and hence central density $\Sigma_0/2h_z$), and scale length h_R. The spherical density profile for the bulge and dark matter halo is given by:

$$\rho_{\text{spheroidal}}(R, z) = \rho_0 \left(\frac{\tilde{r}}{a}\right)^{-\gamma} \left(1 + \frac{\tilde{r}}{a}\right)^{\gamma - \beta} \exp\left[-\left(\frac{\tilde{r}}{r_s}\right)^\alpha\right], \quad (2)$$

with a density normalization ρ_0, a scale radius a, an outer scale radius r_s, and exponents α, β, γ. The ellipsoidal radius is defined as $\tilde{r} = \sqrt{R^2 + \left(\frac{z}{q}\right)^2}$, with q the vertical axis ratio. All parameters are given in Table 1. The baryonic mass of the model is $6 \times 10^{10} \text{M}_\odot$ and the dark matter halo is relatively light, with a mass of $3.1 \times 10^{11} \text{M}_\odot$, in between the typical values obtained from circular velocity curve analyses (e.g., Jiao et al. 2023; Ou et al. 2024) and those obtained from escaped speed curves, satellite dynamics or stream fitting (e.g., Monari et al. 2018; Callingham et al. 2019; Roche et al. 2024; Ibata et al. 2024). Only the mass in the inner Galaxy however matters for our present modelling: the total enclosed mass (baryons and dark matter) within 20 kpc is $2.2 \times 10^{11} \text{M}_\odot$, roughly in agreement with the Malhan & Ibata (2019) constraint. The local dark matter density at the Sun's position is $1.3 \times 10^{-2} \text{M}_\odot \text{ pc}^{-3}$, consistent with most estimates (de Salas & Widmark 2021, and references therein). In the center, the dark matter halo displays a constant density core (with a central power-law slope of 0) as well as a shallow power-law decline close to the center with a slope of -0.6 at $R = 1$ kpc and of -1 at $R = 3$ kpc. All these background potential parameters could in principle be let free in our fitting procedure here-

---

[1] Let $\mathcal{J}$ be the Jacobian of the transformation between $(\boldsymbol{J}, \boldsymbol{\theta})$ and $(\boldsymbol{x}, \boldsymbol{V})$. Since $\det \mathcal{J} = 1$ for canonical variables (Binney & Tremaine 2008), the transformation between a DF in $(\boldsymbol{J}, \boldsymbol{\theta})$, $f(\boldsymbol{J}, \boldsymbol{\theta})$, and the one in $(\boldsymbol{x}, \boldsymbol{V})$, $f'(\boldsymbol{x}, \boldsymbol{V})$, is given by $f'(\boldsymbol{x}, \boldsymbol{V}) = f(\boldsymbol{J}(\boldsymbol{x}, \boldsymbol{V}), \boldsymbol{\theta}(\boldsymbol{x}, \boldsymbol{V})) \det \mathcal{J} = f(\boldsymbol{J}(\boldsymbol{x}, \boldsymbol{V}), \boldsymbol{\theta}(\boldsymbol{x}, \boldsymbol{V}))$, i.e. f' is just f with $\boldsymbol{J}$ and $\boldsymbol{\theta}$ written as functions of $\boldsymbol{x}$ and $\boldsymbol{V}$.

after, but to simplify the problem they have all been fixed to resemble closely the axisymmetric part of the model by Portail et al. (2017). The circular velocity curve corresponding to this axisymmetric model is plotted on the left panel of Fig. 2. The non-axisymmetric modes that will be added on top of this axisymmetric background will all have zero total mass, meaning that the total mass of the final non-axisymmetric model will be the same as that of the axisymmetric one. Since our orbits will be computed strictly within the plane, we only need hereafter the background potential within the plane, $\Phi_0(R)$.

3.2. Axisymmetric equilibrium distribution function

The second step of our procedure consists in choosing an equilibrium DF for the tracer stellar population within the plane. Since we are confined to the plane, we do not attempt here to be fully self-consistent (see, e.g. Binney & Vasiliev 2023), in order to allow for a simple and tractable form of the DF, namely a simple linear combination of two quasi-isothermal DFs $f(J_R, J_\varphi) = F_{\text{thin}} + \zeta F_{\text{thick}}$ with $\zeta = 0.05$, that are two-dimensional and both with the following form (Binney 2010; Binney & McMillan 2011),

$$F = \eta \frac{\Omega(J_\varphi)}{\kappa(J_\varphi)\tilde{\sigma}_R^2(J_\varphi)} \exp\left(-\frac{R_g(J_\varphi)}{h_R}\right) \exp\left(-\frac{J_R \kappa(J_\varphi)}{\tilde{\sigma}_R^2(J_\varphi)}\right), \quad (3)$$

with R_g the guiding radius, Ω, κ the circular and epicyclic frequencies, all three depending on the azimuthal action J_φ, h_R the disk scale length, η the normalization factor (in units of inverse length square) of the tracer population, and finally the radial velocity dispersion $\tilde{\sigma}_R$ depending on the guiding radius as:

$$\tilde{\sigma}_R(R_g(J_\varphi)) = \tilde{\sigma}_R(R_0)\exp\left(-\frac{R_g(J_\phi) - R_0}{h_{\sigma,R}}\right), \quad (4)$$

where $h_{\sigma,R}$ is the kinematic scale-length of the tracer population. For F_{thin}, we set the scale length to $h_R = 2.4$ kpc in accordance with the potential, the velocity dispersion at the Sun's position to $\tilde{\sigma}_{R,\text{thin}}(R_0) = 30$ kms^{-1}, and the kinematic scale length to $h_{\sigma_R} = 10$ kpc. For F_{thick}, the only difference is that we set $\tilde{\sigma}_{R,\text{thick}}(R_0) = 55$ kms^{-1}. The local velocity distribution at $R = R_0$ corresponding to this axisymmetric DF is displayed on the right panel of Fig. 2. In practice, the normalization factor is adjusted such that the number of stars in the model at the Sun is the same as found in the data within 300 pc from the Sun.

3.3. Non-axisymmetric potential

The third step of our procedure is to add non-axisymmetric modes on top of the axisymmetric background potential Φ_0. The total potential is obtained by adding to $\Phi_0(R)$ the real part of the following:

$$\Phi_{\text{tot}}(R, \varphi, t) = \Phi_0(R) + \sum_m \phi_{\text{b},m}(R, t) \exp[\text{i}\, m(\varphi - \varphi_{\text{b},0} - \Omega_{\text{b}}t]$$
$$+ \sum_m \phi_{\text{s},m}(R, t) \exp[\text{i}\, m(\varphi - \varphi_{\text{s},m,0} - \Omega_{\text{s},m}t], \quad (5)$$

where the current phase and the pattern speed of the bar are respectively $\varphi_{\text{b},0}$ and Ω_{b}, and those of the spiral arms mode m respectively $\varphi_{\text{s},m,0}$ (the present-day spiral phase at the Solar position) and $\Omega_{\text{s},m}$. The amplitude of each mode is given by $\phi_{\text{b},m}$ and $\phi_{\text{s},m}$ for the bar and spirals, respectively. The time t is such that currently $t = 0$.

As outlined hereabove, the amplitude of the modes of the bar potential are fixed to values that fit well the dynamics of the bulge region. Namely, the bar potential is a superposition of three Fourier modes, with the same parametric form as in Thomas et al. (2023), closely resembling the three first even modes of the bar potential derived in Portail et al. (2017). From this same potential, the bar angle phase is fixed to be $\varphi_{\text{b},0} = 28°$. The amplitude of each bar mode m is given by:

$$\phi_{\text{b},m}(R, t) = G_{\text{b}}(t) A_{\text{b},m}(R) \Phi_0(R), \quad (6)$$

where $G_{\text{b}}(t)$ is the growth function for the bar, and $A_{\text{b},m}$ is the relative amplitude of the bar mode given by

$$A_{\text{b},m}(R) = K_{\text{b},m} (R/R_{\text{b,max}})^{a_m-1} (1 - R/R_{\text{b,max}})^{b_m-1}, \quad (7)$$

with $K_{\text{b},m}$ a global amplitude factor and $R_{\text{b,max}}$ the radius at which the mode's amplitude goes to zero. Importantly, we consider that the amplitude has reached a plateau at the present time $G_{\text{b}}(t = 0) = 1$. The values of $K_{\text{b},m}$, a_m, and b_m for each of the bar modes are presented in Table 2. Only the pattern speed of the bar is adjusted to the location of resonant ridges in local velocity space within our procedure (see next Section).

The spiral arms potential that we propose is an adaption of the analytical model of Cox & Gomez (2002) described in Monari et al. (2016b), whose amplitude is given by

$$\phi_{\text{s,m}}(R, t) = G_{\text{s,m}}(t) A_{\text{s},m}(R) \exp\left[\text{i}\, m \frac{\ln(R/R_0)}{\tan p_{\text{s},m}}\right] \Phi_0(R), \quad (8)$$

where $G_{\text{s,m}}(t)$ is the growth function for the spiral arms mode m, set to $G_{\text{s,m}}(t = 0) = 1$, $p_{\text{s},m}$ is the pitch angle, and $A_{\text{s},m}$ is given by

$$A_{\text{s},m}(R) = \xi_{\text{s},m}(R) H_m(R) \frac{\Phi_0(R_0)}{\Phi_0(R)}, \quad (9)$$

where $\xi_{\text{s},m}$ is the amplitude factor of the mode, normalized to its value $K_{\text{s},m}$ at $R = R_0$ with a radial dependence as follows:

$$\xi_{\text{s},m}(R) = K_{\text{s},m} \frac{mR_0^2 \sin^2 p_{\text{s},m} + m^2 h_{\text{s},m}R_0 \sin p_{\text{s},m} + 0.3m^3 h_{\text{s},m}^2}{mR^2 \sin^2 p_{\text{s},m} + m^2 h_{\text{s},m}R \sin p_{\text{s},m} + 0.3m^3 h_{\text{s},m}^2}$$
$$\times \frac{R^3 \sin^3 p_{\text{s},m} + 0.3m h_{\text{s},m}R^2 \sin^2 p_{\text{s},m}}{R_0^3 \sin^3 p_{\text{s},m} + 0.3m h_{\text{s},m}R_0^2 \sin^2 p_{\text{s},m}}. \quad (10)$$

This adaptation of the Cox & Gomez (2002) potential has the advantage to be easily generalizable to 3D. Here, $h_{\text{s},m}$ corresponds the scale-height of the spiral potential, which we fix to 130 pc. Finally, H_m is a radial cutoff function, parametrized by an inner and an outer cutoff, respectively, $R_{\text{s},m,\text{min}}$ and $R_{\text{s},m,\text{max}}$. The function is simply:

$$H_m(R) = \begin{cases} 1 & \text{if } R_{\text{s},m,\text{min}} \leq R \leq R_{\text{s},m,\text{max}}, \\ 0 & \text{otherwise.} \end{cases} \quad (11)$$

These cutoffs will be determined from the pattern speeds of the bar and spiral modes in the next Section. The parameters of the spiral arms (for each mode: amplitude $K_{s,m}$, pitch angle $p_{s,m}$, present-day phase at the Solar position $\varphi_{\text{s},m,0}$, and pattern speed $\Omega_{\text{s},m}$) will be adjusted to the data in the next Section, together with the bar pattern speed Ω_{b}.

Table 1. Parameters of the axisymmetric background density used to compute the background potential, following the definitions in Eq. 1 and Eq. 2.

Disky density profiles			
Component	Σ_0 ($10^3 M_\odot$ pc^{-2})	h_R (kpc)	h_z (kpc)
Stellar disk	1.19	2.4	0.30
Gas disk	0.07	4.8	0.13

Spheroidal density profiles							
Component	ρ_0 ($10^{-1} M_\odot$ pc^{-3})	a (kpc)	r_s (kpc)	α	β	γ	q
Bulge	1.08	8.16	0.83	2.0	2.9	1.3	1.0
DM halo	4.56	–	0.65	0.50	0.0	0.0	0.8

Table 2. Parameters of the planar fiducial non-axisymmetric potential fitted in Sect. 4.2, with parameters as defined in Eqs 7 and 9.

Bar											
Ω_b	$\varphi_{b,0}$	$R_{b,max}$	$K_{b,2}$	$K_{b,4}$	$K_{b,6}$	a_2	a_4	a_6	b_2	b_4	b_6
37 kms^{-1}kpc^{-1}	28°	12 kpc	0.25	8.4	210.41	1.8	4.08	5.96	5.08	10.7	16.06

$m=2$ spiral									
$\Omega_{s,2}$	$K_{s,2}$	$\varphi_{s,2}$	$p_{s,2}$	$R_{s,2,min}$	$R_{s,2,max}$	$h_{s,2}$	$\Sigma_{s,2}$	ILR	CR
13.1 kms^{-1}kpc^{-1}	0.15 %	47.8 °	8.1 °	6.6 kpc	26.4 kpc	0.13 kpc	24.9 %	4.1 kpc	17.6 kpc

$m=3$ spiral									
$\Omega_{s,3}$	$K_{s,3}$	$\varphi_{s,3}$	$p_{s,3}$	$R_{s,3,min}$	$R_{s,3,max}$	$h_{s,3}$	$\Sigma_{s,3}$	ILR	CR
16.4 kms^{-1}kpc^{-1}	0.06 %	81.7 °	13.7 °	8.0 kpc	19.6 kpc	0.13 kpc	9.3 %	8.0 kpc	14.4 kpc

4. Fitting procedure and results

4.1. Bar-only model

With all the parametric components of the potential defined above, we are now in a position to launch our backward integrations to adjust the parameters to the data. As outlined hereabove, the amplitude of the modes and the phase of the bar potential are fixed to values that fit well the dynamics of the bulge region. Only the pattern speed of the bar will now be adjusted to the location of resonant ridges in local velocity space, excluding the spiral arms from the model.

Another hyper-parameter to fix is the (dummy) integration time, T_{int}, within the backward integration context. This will not affect the location of ridges in local velocity space but will affect their apparent "sharpness". As in Dehnen (2000), we separate the total integration time into two equal-time phases of growth of the bar and plateau of its amplitude, with the following growth function:

$$G_b(t) = \begin{cases} 1 & \text{if } -\frac{T_{int}}{2} \leq t \leq 0, \\ \frac{3}{16}\mathcal{T}^5 - \frac{5}{8}\mathcal{T}^3 + \frac{15}{16}\mathcal{T} + \frac{1}{2} & \text{if } -T_{int} < t < -\frac{T_{int}}{2}, \end{cases} \quad (12)$$

where $\mathcal{T} \equiv (4t + 3T_{int})/T_{int}$. We choose to adjust those two parameters (pattern speed and dummy integration time) to the 1-D distribution of stars in the Solar neighborhood for azimuthal velocities within 90 kms$^{-1} < V_\varphi < 330$ kms^{-1} at $V_R = 100$ kms^{-1}. This distribution is shown in Fig. 3. The choice of analyzing the ridges at high V_R prevents them from being "contaminated" by the additional effect of spiral arms since, as we shall see in the next subsection, these distort local velocity space mostly in the central regions of the velocity ellipsoid. This adjustment of the bar pattern speed is made in the Solar neighborhood, which is the most complete volume, so that peaks and valleys are not missing.

Quantitatively, we compare the sum of the squares of the differences of the 1-D distribution of azimuthal velocities on each bin of 2 kms^{-1} between the Gaia RVS disk sample and the bar-only model. Only the location of the peaks matters here, so the DF renormalization is applied only in the small V_R range considered on Fig.3, instead of the DF normalization applied within the whole local velocity space in all other instances. We find the best match at $\Omega_b = 37$ kms^{-1}kpc^{-1} for a total (dummy) integration time of 543 Myr corresponding to 3.2 rotations of the bar. Note however that the velocity peak that can be attributed to Bobylev moving group, or lower part of the Hercules bimodality (at $V_\varphi \sim 160$ kms^{-1} on Fig. 3), is not recovered, and is never so by a bar-only model that also reproduces the hat at large V_φ. Our best value of the pattern speed places the corotation radius of the bar at $R = 6.6$ kpc and its OLR radius at $R = 11$ kpc.

On the first column of Fig. 4, we display the distribution of (V_R, V_φ) velocities in the Solar neighbourhood (setting the value to zero in pixels with no stars in the data), of the local (J_φ, J_R) action distribution, as well as the median Galactocentric radial velocity $\tilde{V}_R$ as a function of position within the Galactic plane. Remarkably, the local kinematic distribution corresponding to this *bar-only* model is already very similar to the observed one, without any additional contribution from spiral arms (see also Monari et al. 2019b, for a less quantitative but similar conclusion). The success of this bar model at producing so many features resembling the observed local kinematic distribution comes from the signatures of the Lindblad resonances of its multiple modes. We confirm this in the Appendix, where we provide a simple formula based on constant energy lines within the improved epicyclic formalism of Dehnen (1999a) in order to evaluate the approximate location of the signature of each bar resonance in local velocity space. At $V_R = 100$ kms^{-1}, these approximate locations of the bar resonances are also indicated as small dashes on top of Fig. 3. However, as it also appears clearly in the third row of Fig. 4, the bar-only model produces a dipolar structure of median radial velocities within the plane, far from the observed one. This implies
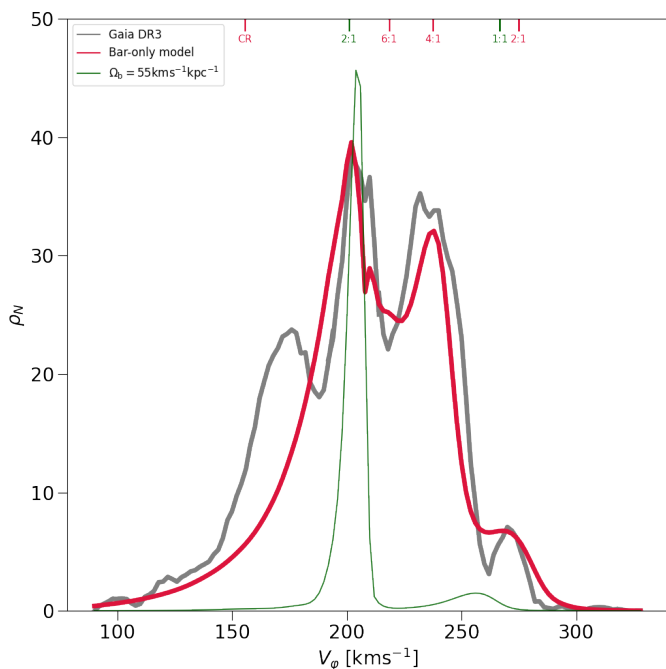
Fig. 3. 1-D distribution of the azimuthal velocity of stars in the Solar neighborhood within 99 $\mathrm{kms}^{-1} < V_R < 101$ kms^{-1}, a region of velocity space where the bar impact dominates the distribution (over potential spiral arms signatures). In grey, the stellar distribution from the Gaia RVS disk sample in the Solar neighbourhood, smoothed with the Savitzky-Golay filter from the `SciPy` library. Red line: the renormalized best bar-only model at $V_R = 100$ kms^{-1}, with pattern speed $\Omega_\mathrm{b} = 37$ $\mathrm{kms}^{-1}\mathrm{kpc}^{-1}$. For reference, we are providing the results for $\Omega_\mathrm{b} = 55$ $\mathrm{kms}^{-1}\mathrm{kpc}^{-1}$ (green line), where only the 1:1 resonance leaves a small signature at higher V_φ than the strong OLR peak. The approximate locations of the different resonances evaluated from Eq. A.5 are represented as red ($\Omega_\mathrm{b} = 37$ $\mathrm{kms}^{-1}\mathrm{kpc}^{-1}$) and green ($\Omega_\mathrm{b} = 55$ $\mathrm{kms}^{-1}\mathrm{kpc}^{-1}$) dashes on top of the plot.

that other dynamical ingredients are required to reproduce this median velocity field, which will be the topic of the following subsection. Another clear defect of the bar-only model, locally, is that the Sirius moving group does not stand out in local velocity space. Quantitatively, if one considers the density of stars within a strip of V_φ between 250 kms^{-1} and 260 kms^{-1} in local velocity space, and compares the value at $V_R = -12$ kms^{-1} to that at $V_R = 0$ kms^{-1}, one gets an increase of ∼25% in the data at $V_R = -12$ kms^{-1} (the Sirius peak), while one gets a *decrease* of 11% in the bar-only model (almost identical to the axisymmetric case). This indicates that Sirius is likely caused by spiral arms.

4.2. Adding spiral arms

Given the failure of the bar-only model to reproduce the median radial velocity field, the next step is to add non-axisymmetric modes corresponding to spiral arms. We start by adding a single mode on top of the bar-only model (i.e., with now fixed $\Omega_\mathrm{b} = 37$ $\mathrm{kms}^{-1}\mathrm{kpc}^{-1}$), with multiplicity $m \in [1, 2, 3, 4]$. We fix the scale height to be the same as that of the gas component of the background potential, $h_{\mathrm{s},m} = 130$ pc, the outer cut-off to be the OLR of the spiral, and the inner cut-off to be the larger between the corotation radius of the bar and the ILR of the spiral (so that the spiral lives between its ILR and OLR but does not penetrate within the corotation of the bar). The growth function $G_{\mathrm{s},m}(t)$

has the same form as the bar, and we fix the integration time to exactly one full rotation of the spiral arm mode. In many other attempts, even allowing more than one rotation and a different growth time, the best candidates in the method that follows tend to converge close to the preferred values we found.

The exploration of the whole parameter space with the backward integration method over a large portion of phase-space is computationally very costly, which led us to select the following strategy to fit the Galaxy model to the Gaia data. The fit is realized with the differential evolution method of Storn & Price (1997), a global genetic optimization method implemented in the Python `SciPy` library. This algorithm minimizes an objective function, set to be a weighted error function $\mathcal{L} = \sum_i (\tilde{V}_{R,i}^{\mathrm{model}} - \tilde{V}_{R,i}^{\mathrm{data}})^2 / \sigma_i^2$, comparing median radial velocities from model and data on a small selection of points (x_i, y_i) with weights $1/\sigma_i$. The observed median radial velocities $\tilde{V}_{R,i}^{\mathrm{data}}$ are calculated within bins of size 250 pc around the selected point (x_i, y_i), whilst the model median radial velocities are the median of the V_R distribution at the selected point, i.e. the model DF values in the (V_R, V_φ) plane integrated over V_φ. The choice of the selected points and their respective weights is a delicate one. The number of points must be limited, in order to limit the computation time, but this also means that they must be chosen at 'strategic' positions and not simply on a uniform grid. Moreover, simply weighting them by the number of stars in the data would give too much weight to the Solar vicinity over the entire area of the fit. The first point to which we nevertheless still give the highest weight, $1/\sigma_0$ is the Solar position (x_0, y_0). We then need to choose points which are representative of the variations of the (positive and negative) values of the median radial velocity all over the plane. Adding spiral arms invariably runs the risk of not preserving the roughly correct radial velocity gradient from the bar in the region around $(x_1, y_1) = (7.0\,\mathrm{kpc}, 3.5\,\mathrm{kpc})$ and $(x_2, y_2) = (7.0\,\mathrm{kpc}, 1.0\,\mathrm{kpc})$, but it is needed to change the sign of $\tilde{V}_R$ at $(x_3, y_3) = (9.0\,\mathrm{kpc}, 0.0\,\mathrm{kpc})$. These are our three second-most important points, all with $\sigma_i = 2\sigma_0$. We then choose two pairs of points along constant y axes that encapsulate the positive-negative variations of the median radial velocity field, $(x_4, y_4) = (6.5\,\mathrm{kpc}, 0.0\,\mathrm{kpc})$, $(x_5, y_5) = (10.0\,\mathrm{kpc}, 0.0\,\mathrm{kpc})$, $(x_6, y_6) = (7.0\,\mathrm{kpc}, -3.0\,\mathrm{kpc})$, and $(x_7, y_7) = (10.0\,\mathrm{kpc}, -3.0\,\mathrm{kpc})$, with $\sigma_i = 3\sigma_0$. In order to capture the clear spiral feature at the bottom-left of the plane, we also add two points, $(x_8, y_8) = (6.0\,\mathrm{kpc}, -2.5\,\mathrm{kpc})$ and $(x_9, y_9) = (7.5\,\mathrm{kpc}, -2.5\,\mathrm{kpc})$, with $\sigma_i = 5\sigma_0$. We finally impose a constraint in the outer disk, $(x_{10}, y_{10}) = (11.5\,\mathrm{kpc}, 1.0\,\mathrm{kpc})$ and $(x_{11}, y_{11}) = (12.0\,\mathrm{kpc}, 0.0\,\mathrm{kpc})$, also with $\sigma_i = 5\sigma_0$. These are the essential points of our fit. We add on top of this a set of low-weight points that will merely help guiding the fit, $(x_{12}, y_{12}) = (9.0\,\mathrm{kpc}, -3.0\,\mathrm{kpc})$, $(x_{13}, y_{13}) = (9.0\,\mathrm{kpc}, 3.5\,\mathrm{kpc})$, $(x_{14}, y_{14}) = (10.0\,\mathrm{kpc}, 3.5\,\mathrm{kpc})$, and $(x_{15}, y_{15}) = (12.0\,\mathrm{kpc}, 3.5\,\mathrm{kpc})$, all with $\sigma_i = 100\sigma_0$. All the selected points are indicated as squares on the bottom-middle panel of Fig. 4. This selection of points and their weights hereafter plays the role of a prior on what the most important regions of configuration space are.

For our genetic algorithm, let us now define our population of candidate solutions in parameter space as $\mathbf{a}_{i,g}$, with $1 \le i \le n$ and $1 \le g \le N$. This means we will consider n candidates at each generation, for N generations. In practice, a first generation of candidate solutions is created by picking stochastically many candidate parameters across parameter space, all while trying to cover most of the parameter space. This population is then mutated, candidate by candidate, iteratively, thereby establishing a new generation at each iteration. At each generation g, the muta-
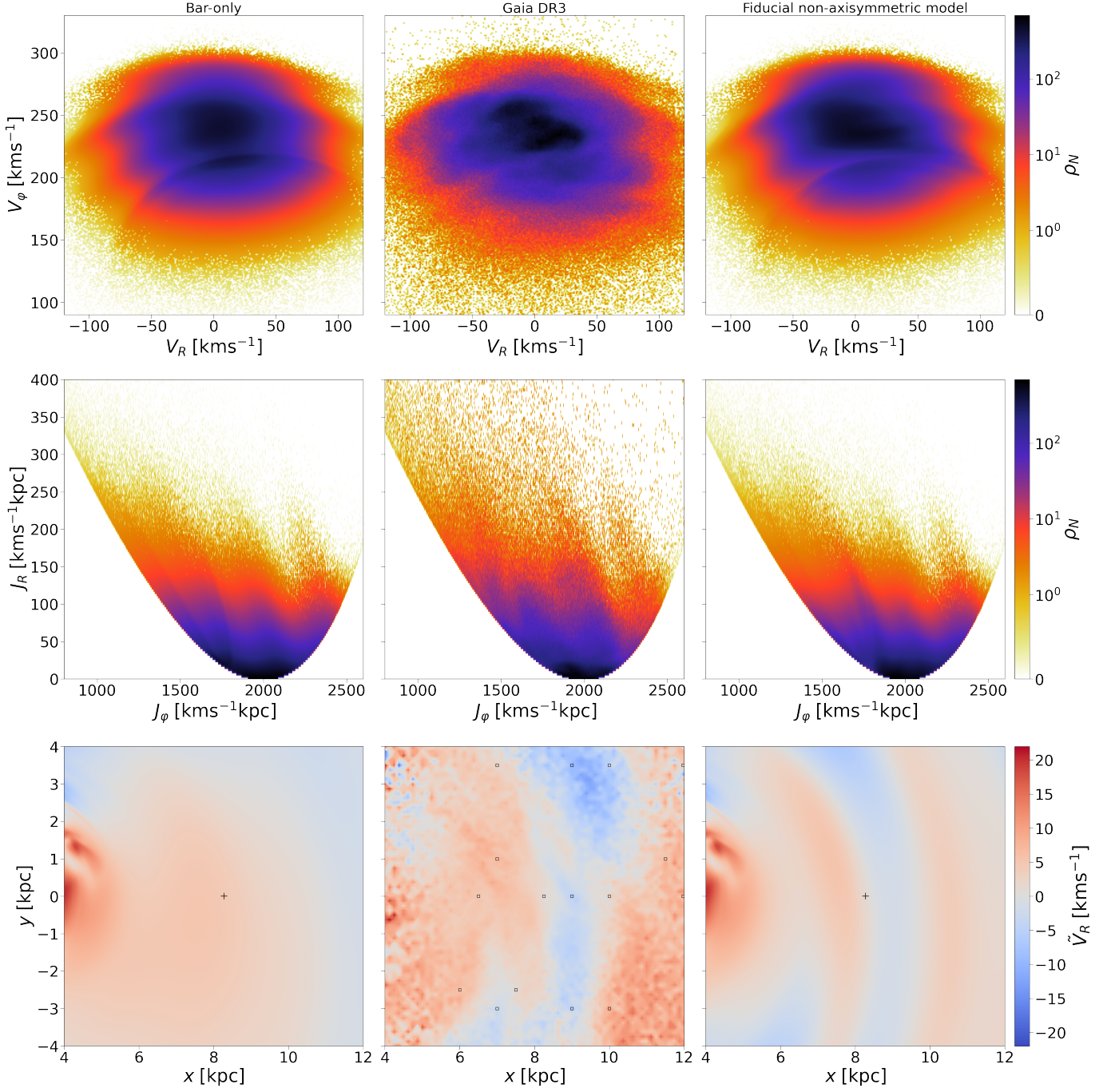
Fig. 4. From left to right, the columns correspond to the bar-only model, the Gaia RVS disk sample and our fiducial non-axisymmetric model, respectively. Top row: the 2-dimensional histogram of stars on the local (V_R, V_φ) plane defined on $[-200, 200]$ kms^{-1} × $[0, 400]$ kms^{-1}, binned with bins of size $(1$ kms$^{-1})^2$. Middle row: the 2-dimensional histogram of the number density of stars on the (J_R, J_φ) plane defined on $[0, 400]$ kms^{-1}kpc^{-1} × $[800, 2600]$ kms^{-1}kpc^{-1}, binned with bins of size $(3 \times 2$ km^2 s^{-2}kpc$^{-2})$. For this, the velocities (V_R, V_φ) have been transformed to actions (J_R, J_φ) with AGAMA. Bottom row: the median $\tilde{V}_R(x, y)$ is shown in the (x, y) plane defined on $[4, 12]$ kpc × $[-4, 4]$ kpc, and binned with bins of size $(125$ pc$)^2$ for the data and $(50$ pc$)^2$ for the models. The cross locates the Sun and squares on the middle panel (data) indicate the selected points where the fit has been performed. All panels were smoothed with a bi-linear interpolation.

tion of each candidate $\mathbf{a}_{i,g}$ is applied according to the "best1bin" strategy with the following steps:

- Select the best parameters candidate (the one minimizing the weighted error function at current generation), $\mathbf{a}_{best,g}$.

- To mutate each candidate $\mathbf{a}_{i,g}$, randomly select two other parameters vector candidates, $\mathbf{a}_{j,g}$ and $\mathbf{a}_{k,g}$.

- Take a fixed multiplication factor (mutation factor $\mathcal{M}$) of their difference in parameters, $\mathcal{M}(\mathbf{a}_{j,g} - \mathbf{a}_{k,g})$ to get a vector $\mathbf{v}_i = \mathbf{a}_{best,g} + \mathcal{M}(\mathbf{a}_{j,g} - \mathbf{a}_{k,g})$

- The new trial vector $\mathbf{a}_{i,g+1}$ is then built component by component by assigning the value of each parameter either from $\mathbf{v}_i$ or from $\mathbf{a}_{i,g}$ according to if a realization of the binomial function between 0 and 1 is smaller or greater than a chosen recombination value C, respectively.
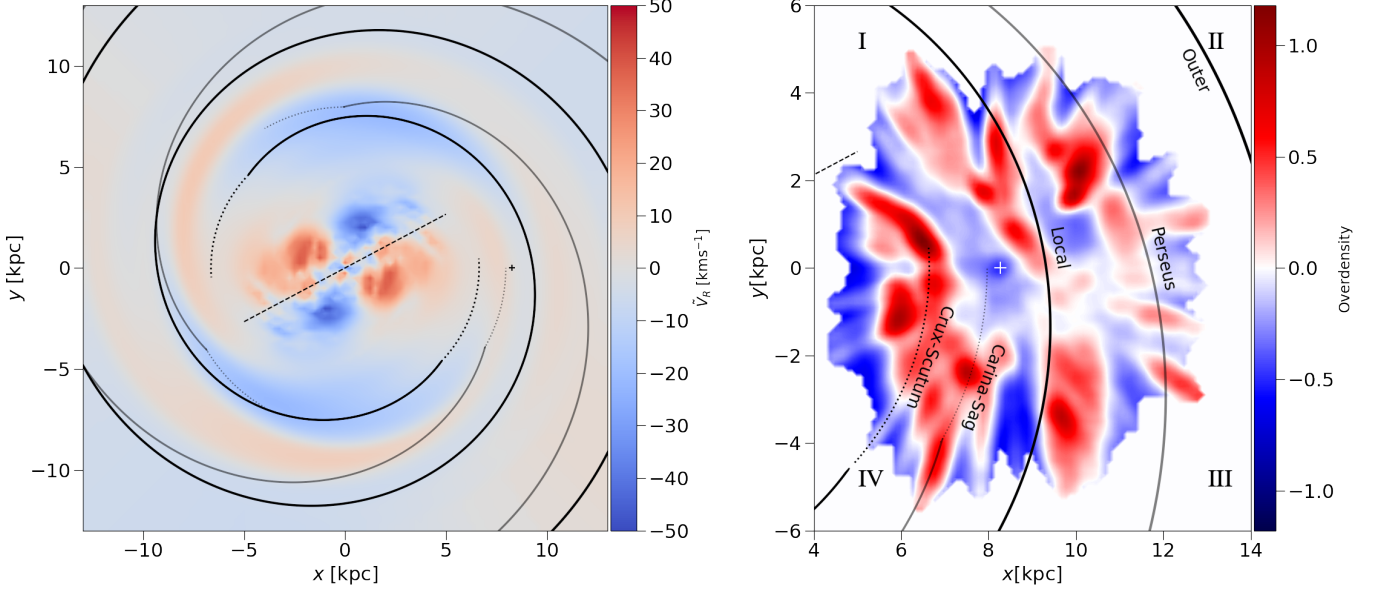
Fig. 5. Left panel: Median radial velocity $\tilde{V}_R$ for the fiducial non-axisymmetric model on the disk plane (x, y) defined on $[-13, 13]$ kpc $\times$ $[-13, 13]$ kpc binned with $(250 \text{ pc})^2$ bins. Right panel: Adaptation of panel B in figure 1 of Poggio et al. (2021) with over-densities of young upper main sequence stars in red tracing the position of the arms segments. Both panels display the bar position of our fiducial model with dashed black lines, the major $m = 2$ (black) and minor $m = 3$ (grey) spiral locations of our fiducial model as continuous and dotted black and gray lines, respectively (the dotted line indicates that the maximum overdensity of the model spiral has reached inside the inner cut-off, but that there is still an overdensity in the model, indicated by the dotted line and reaching zero where the dotted line stops). In both panels, the cross represents the Sun's position. The overdensity maps of young stars following Poggio et al. (2021) are generated from `https://github.com/epoggio/Spiral_arms_EDR3.git`.
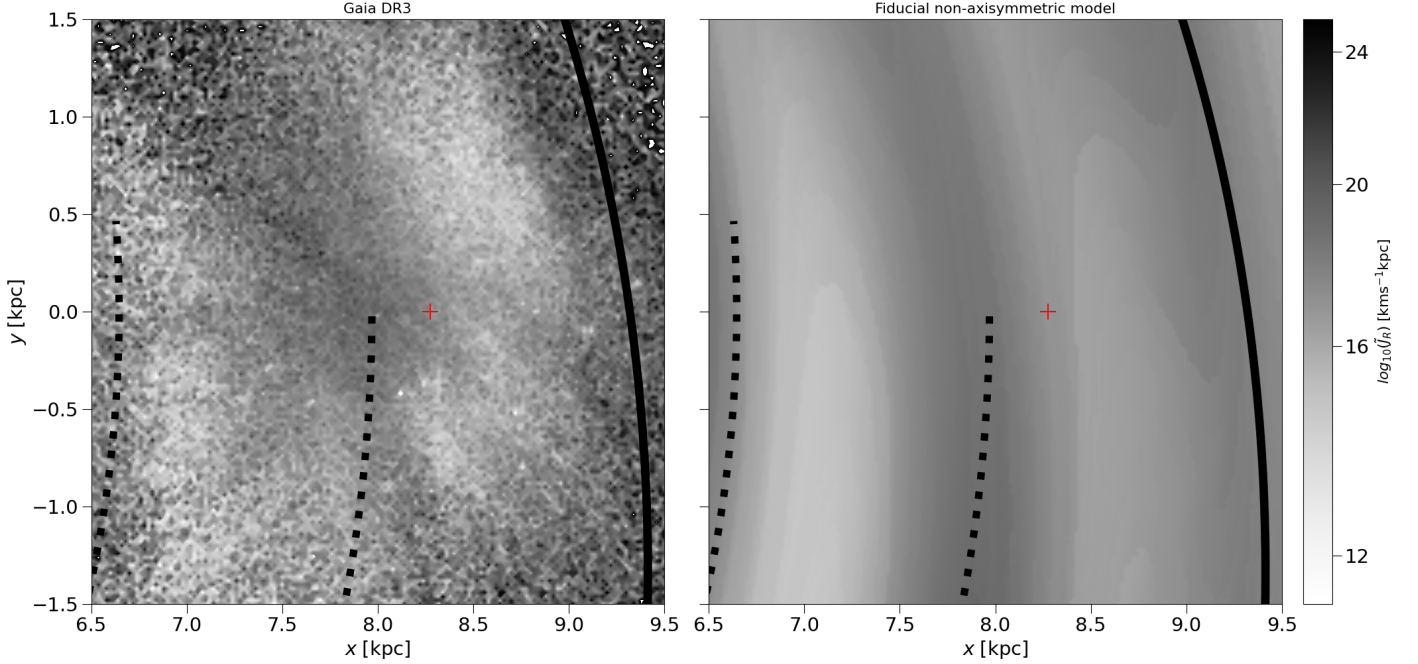
Fig. 6. The median J_R as a function of position in the data of the extended Solar neighbourhood (left panel) and in the model (right panel). The lines indicate the location of spiral arm segments in the model and the red cross indicates the Sun's position.

— Compute the weighted error function for the trial vector $\mathbf{a}_{i,g+1}$: if it performs better in terms of the objective function, it replaces the original candidate in the next generation, otherwise the initial candidate $\mathbf{a}_{i,g}$ remains the same at generation $g + 1$.

— The convergence criteria are met when the standard deviation of the population objective function values at a given generation is smaller than 1% of the mean objective function value of all candidates in the population in that generation. The final $\mathbf{a}_{best,g=N}$ candidate is kept.
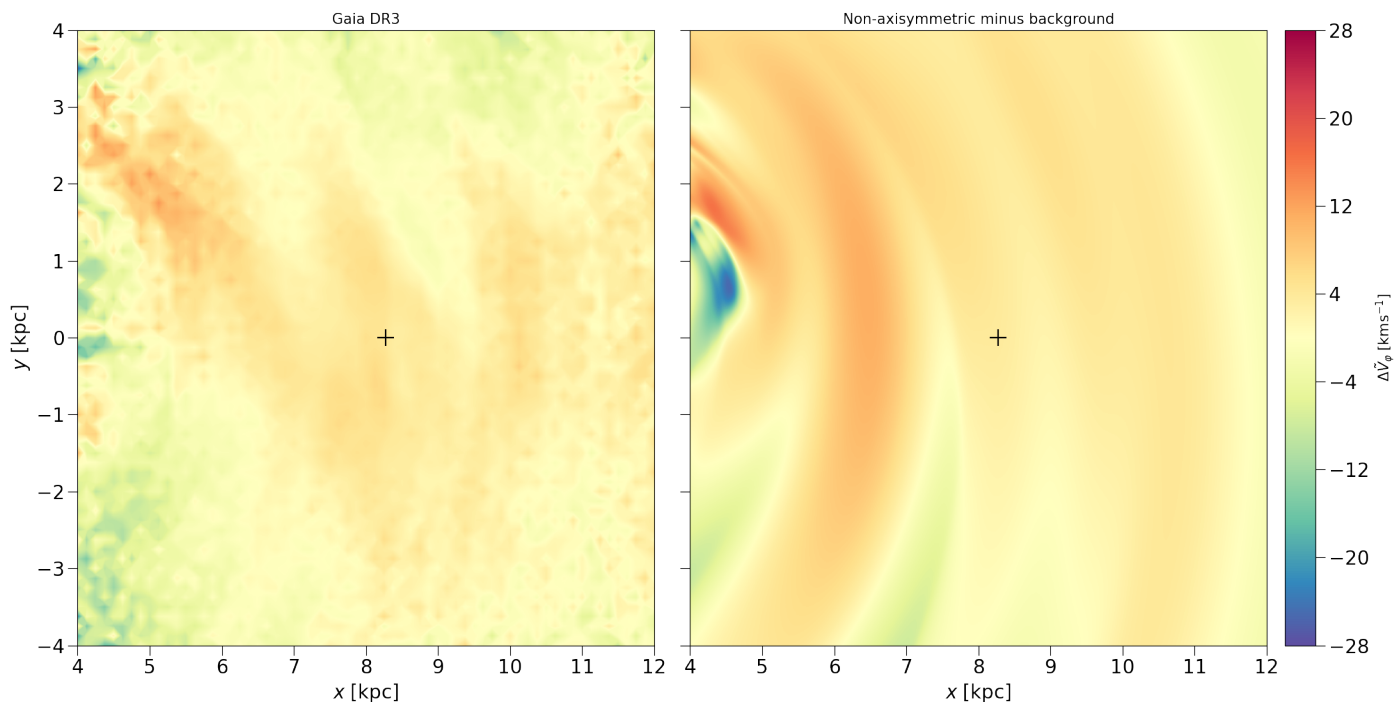
Fig. 7. Left panel: difference of the median azimuthal velocity compared to its average value at fixed R in the Gaia RVS data, $\Delta \tilde{V}_\varphi \equiv \tilde{V}_\varphi(x,y) - \tilde{V}_\varphi(R)$, on the (x,y) plane defined on $[4, 12]$ kpc $\times [-4, 4]$ kpc, binned with $(125 \text{ pc})^2$ bins. Right panel: difference between the median azimuthal velocity of the fiducial model and that of the background axisymmetric DF. In both panels, the black cross indicates the Sun's position.

We kept the standard values of the algorithm hyper-parameters, notably population size n (15 times the number of parameters), the recombination value C, and the mutation factor $\mathcal{M}$. This method was chosen since it is extremely efficient at converging efficiently over a large parameter space. the selection of points and their weights plays the role of a prior on what the most important regions of configuration space are. However, contrary to a classical Bayesian method no posterior or well-defined error bars can be given. Therefore, we are not in a position to provide error bars, and we cannot exclude that our best candidate models found hereafter may be local minima in parameter space. Further improvements of the present work should address this question together with taking into account a Gaia selection function (e.g., Castro-Ginard et al. 2023).

From attempts to fit only one spiral arms mode, the mode $m = 2$ performed the best in terms of the objective function among $m \in [1, 2, 3, 4]$, with a pattern speed of 13 kms^{-1}kpc^{-1}. This is the main result of our search, which we will now seek to refine. Indeed, this preferred single mode model clearly produces a distorted local velocity space, especially a very distorted Sirius-like moving group compared to observations. This is not entirely surprising, as local velocity space has not been used to constrain the fit. We then modify the objective function $\mathcal{L}$ with a local constraint, as follows: $\mathcal{L}' = \mathcal{L} + \sum_{i=1}^{i=2} (\Delta_i^{\text{model}} - \Delta_i^{\text{data}})^2 / \sigma_\Delta^2$, where Δ_0 is the location of the 1-D V_R distribution peak at $V_\varphi = 250$ kms^{-1} ($i = 1$) and at $V_\varphi = 260$ kms^{-1} ($i = 2$) at the Sun, and $\sigma_\Delta = 3\sigma_0$ in both cases. Using $\mathcal{L}'$ however still leads to a best candidate with a distorted Sirius moving group in local velocity space when considering a single $m = 2$ mode.

Then, in order to possibly improve over this model, we attempt a new fit that adds a second spiral mode with multiplicity $m = 3$ or $m = 4$, together with the the first one and the bar. We assume the $m = 2$ spiral to have a range of pattern speeds 10 kms^{-1}kpc^{-1} < $\Omega_{s,2}$ < 14 kms^{-1}kpc^{-1}, close to the

value found for the single mode fit which we aim to improve upon. To reduce the parameter space, the amplitude of the second higher mode, whose pattern speed and pitch angle are allowed to vary, is fixed with the equation proposed by Hamilton (2024), relating the respective amplitude of both modes to their pattern speed and pitch angle, namely as being inversely proportional to the product of their pattern speed squared with the tangent of their pitch angle (hence a higher amplitude for lower pattern speed and lower pitch angle). To further reduce parameter space, we impose that the sum of the local density contrasts for both spiral modes is smaller than 35%, checking a posteriori that this limit will not be reached by our best candidate. To compute the surface density contrast of each mode, we take the ratio between the integrated surface density at the Sun of the axisymmetric baryonic component and the spiral arms surface density corresponding to the Cox & Gomez (2002) potential (see also Monari et al. 2016b). In our analysis we found that the secondary $m = 3$ spiral mode does complement the stronger mode better than the $m = 4$ one in terms of the objective function. Adding this second $m = 3$ mode allowed us to taper and regularize the signature of the Sirius moving group in local velocity space while improving slightly the median radial velocity map. To further polish the parameters of this best candidate found with our global optimization method, we then perform a fine search with a gradient descent in a narrow range of parameter space (1 kms^{-1}kpc^{-1} wide in pattern speed, 6° wide in phase, 2° wide in pitch angle and 0.04% wide in potential amplitude $K_{s,2}$) around our best candidate solution, with the Limited-memory Broyden–Fletcher–Goldfarb–Shanno (L-BFGS-B) algorithm implemented in `Scipy`. The solution thus found constitutes our fiducial model.

The final parameters of this fiducial model are presented in Table 2, while its local velocity and action space distribution, and median radial velocity map, are presented in the third col-
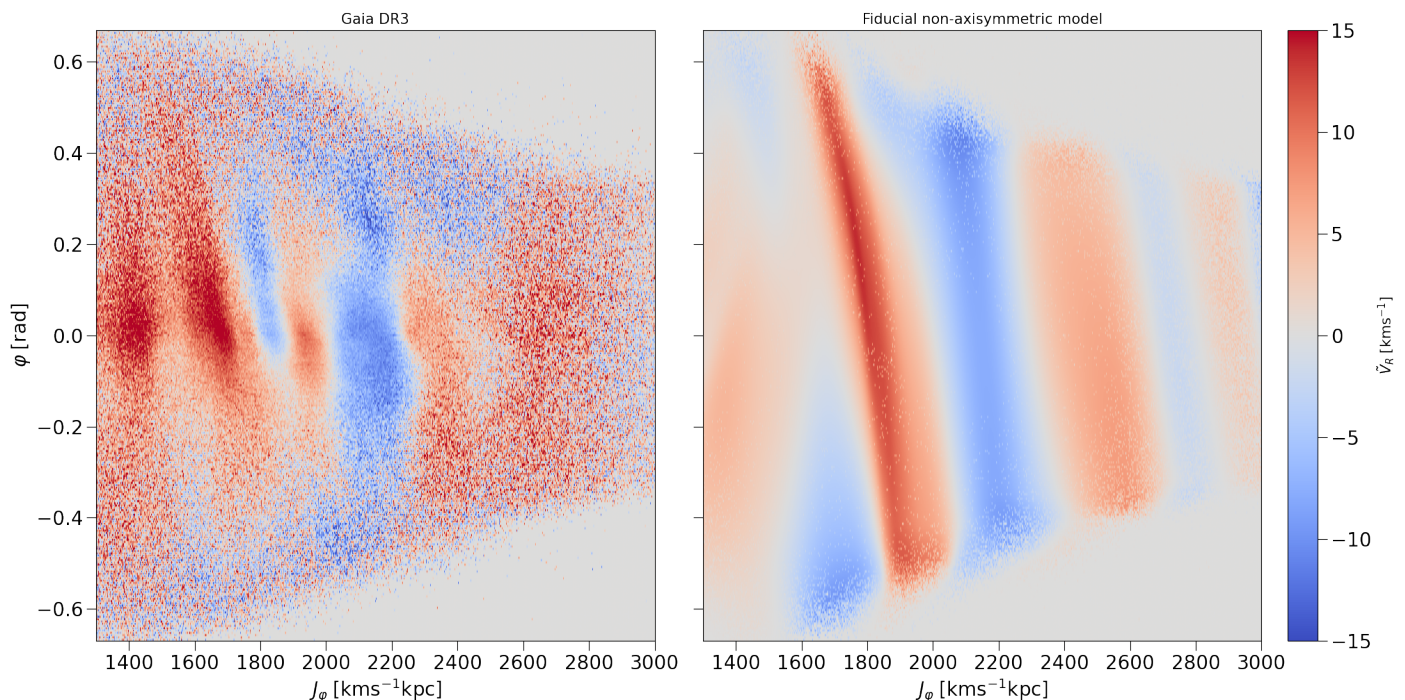
Fig. 8. Median radial velocity on the (φ, J_φ) plane defined on $[-0.78, 0.78]\,\text{rad} \times [1000, 3000]\,\text{kms}^{-1}\text{kpc}^{-1}$, binned with bins of size $(0.005 \times 2.5\,\text{rad} \times \text{kms}^{-1}\text{kpc}^{-1})$. Left panel: the Gaia RVS disk sample. Right: the fiducial non-axisymmetric model. Points outside $5\,\text{kpc} < x < 12\,\text{kpc}$ and $-4\,\text{kpc} < y < 4\,\text{kpc}$ are excluded in both the data and model.

umn of Fig. 4. The improvement of the median radial velocity map compared to the bar-only model is striking, but there are also subtle improvements in local velocity space, in particular a better representation of moving groups close to the center of the velocity ellipsoid. For Sirius, if one reconsiders the density of stars within a strip of V_φ between $250\,\text{kms}^{-1}$ and $260\,\text{kms}^{-1}$, one now gets an *increase* of 5% at $V_R = -12\,\text{kms}^{-1}$ compared to $V_R = 0\,\text{kms}^{-1}$ in the model. This is still a significantly smaller peak than in the data ($\sim$25%), which will require further investigations, but it is a significant improvement upon the *decrease* of 11% in the bar-only model. We will now qualitatively compare the predictions of this fiducial model to other observables in the next Section.

5. Predictions and applications of the model

The fiducial model presented in Table 2 has been adjusted to data with zero prior on the spiral arms locations. One can now check how well the model performs in recovering the position of known spiral arms of the Galaxy, as well as how it fares in reproducing other observables, such as the azimuthal velocity field or the detailed locations of moving groups across the disk.

5.1. Locations of spiral arms

On Fig. 5, we present the global radial velocity map predicted by our fiducial model, together with the location of the bar and of the maximum density of the two dynamically-fitted spiral arm modes. We also compare the location of those arms to the over-densities of young upper main sequence stars identified in Poggio et al. (2021). As it appears clearly on this figure, the strongest $m = 2$ mode nicely matches the location of the Crux-Scutum arm close to the Galactic bar, of the Local arm close to the Sun, and of

the Outer arm. This is also in line with the findings of Widmark & Naik (2024) who found the Local arm to be a strong local over-density, with a contrast density of roughly 20%, close to the local over-density of 24.9% within our model. Since the pattern speed of the $m = 2$ spiral is smaller than that of the bar, this could be interpreted as a recent disconnection (52.5 Myr ago) from the bar in the Crux-Scutum region, in accordance with the findings of Vislosky et al. (2024). On the other hand, the weaker $m = 3$ spiral nicely matches the location of the Carina-Sagittarius and Perseus arms. It is remarkable that a purely dynamical fit mostly recovers the location of known spiral arm over-densities within the disk.

Another interesting quantity to compare our model predictions with is the median J_R as a function of position in the disk. Indeed, Palicio et al. (2023) identified spiral arm structures in the disk from the median $\tilde{J}_R$ values as a function of position. We reproduce such a map from the Gaia RVS data within the extended Solar neighbourhood, in Fig. 6, and overlay the location of the spiral arms from our fiducial model. We also compute the median axisymmetric $\tilde{J}_R$ values from our model, starting from the same grid of velocities as before at each location in the plane, then computing the corresponding radial actions with AGAMA, and summing up the DF values to compute the median. Again, the a posteriori qualitative agreement with the data is remarkable. Note that the increase in median axisymmetric $\tilde{J}_R$ is positively associated to the presence of spiral arms in our model, in accordance with the findings of Debattista et al. (2024) when considering instantaneous axisymmetric actions. In N-body simulations, one typically needs to average actions over a long-enough timescale to even better track the spirals for *low* values (Debattista et al. 2024) of the median time-averaged radial action. In our case, the important takeaway is the a posteriori qualitative agreement between the data and model for the
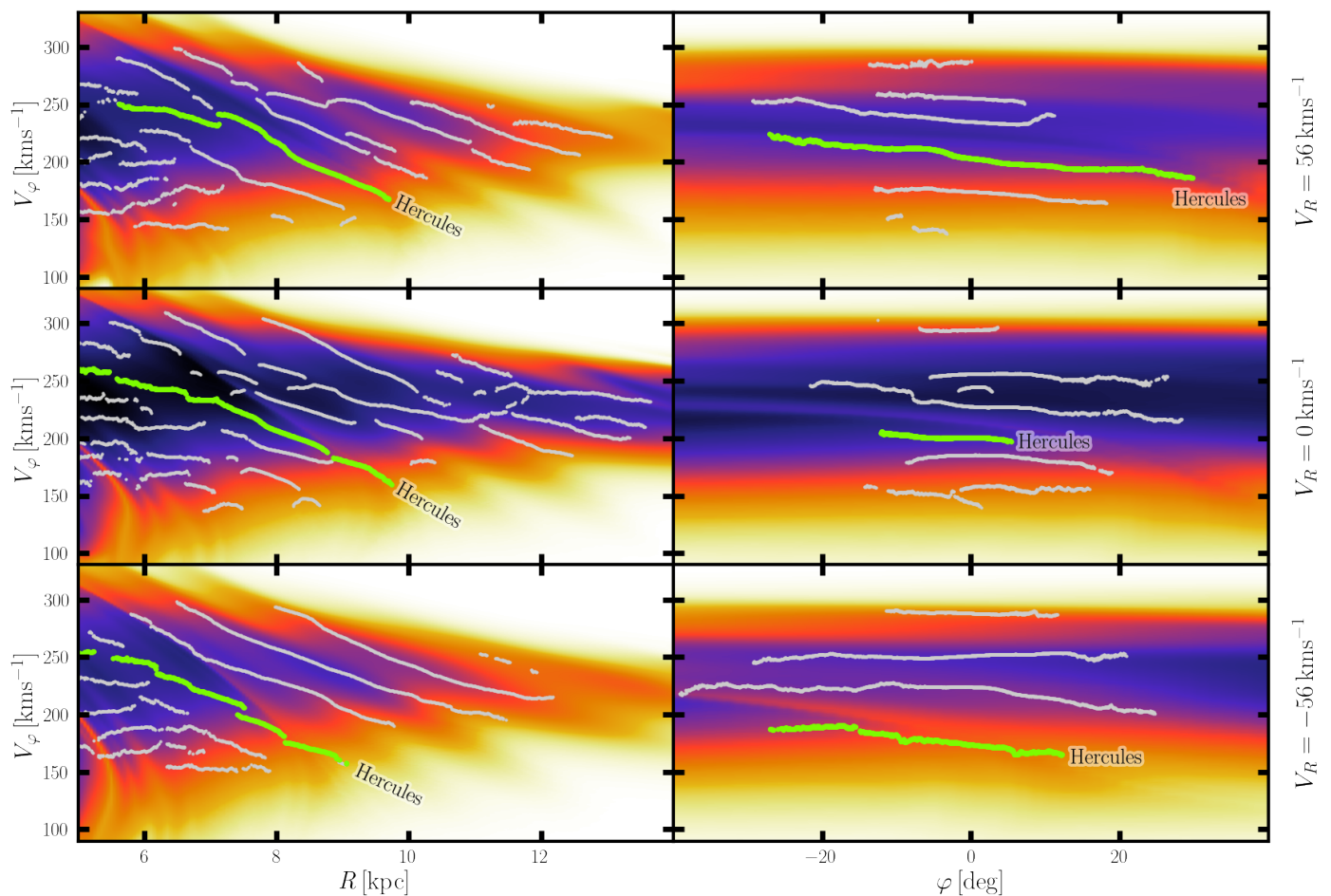
Fig. 9. At fixed V_R for each row ($V_R = 56\,\mathrm{kms}^{-1}$, $V_R = 0\,\mathrm{kms}^{-1}$ and $V_R = -56\,\mathrm{kms}^{-1}$, the white (and green) lines display the main ridges identified in Gaia DR3 *data* with the method developed in Bernet et al. (2022, 2024). Below these lines, we underlay the 2-D histogram distribution of the normalized fiducial model. Left: at fixed azimuth $\varphi = 0°$. Right: at fixed radius $R = R_0$. The Hercules ridge is denoted by a thicker green line.

instantaneous $\tilde{J}_R$, without having used this quantity in the fitting procedure.

5.2. Azimuthal velocity field

An interesting quantity to look at in principle is the variation of the median azimuthal velocity at fixed Galactocentric radius, as this is also a clear signature of the non-axisymmetry of the potential. To avoid being dominated by the background DF and axisymmetric potential, one can plot from the data the value $\Delta\tilde{V}_\varphi \equiv \tilde{V}_\varphi(x,y) - \tilde{V}_\varphi(R)$, on the (x,y) plane. This is shown on the left panel of Fig. 7. One drawback of showing this quantity is that the azimuthal concatenation at fixed R can only be done in the region where data are available, which is why it was not obvious how to implement such a quantity as a target for the fit itself. From our fiducial model, on the other hand, one can directly subtract from the median radial velocity at each position the median radial velocity obtained from the background DF at the same location. Similar trends to the data can be seen, although the two quantities are not straightforward to compare quantitatively.

5.3. Median radial velocity in the azimuth-angular momentum plane

An interesting projection of Gaia data (see, e.g., Friske & Schönrich 2019; Monari et al. 2019a; Trick et al. 2021; Chiba et al. 2021) is the structure of median (or mean) radial velocity in the azimuth-angular momentum plane. In Fig. 8, we display the median radial velocity on the (J_φ, φ) plane for stars within a box $[1300, 3000]\,\mathrm{kms}^{-1}\,\mathrm{kpc} \times [-0.67, 0.67]\,\mathrm{rad}$, within $5\,\mathrm{kpc} < x < 12\,\mathrm{kpc}$ and within $-4\,\mathrm{kpc} < y < 4\,\mathrm{kpc}$. To compute the median values in the model, we first fix an azimuth φ_i every $0.01\,\mathrm{rad}$, then consider radii R_j spaced $10\,\mathrm{pc}$ from one another. Next, for each point we compute the DF with the backward integration method for different velocities V_R and $V_{\varphi,n} = \frac{J_{\varphi,n}}{R_j}$. We then fix $J_{\varphi,n}$ and sum the values of the DF for all radii R_j, and we compute the median radial velocity for each $(\varphi_i, J_{\varphi,n})$. The qualitative agreement with the data is acceptable, although one can note that the signatures become weak at low J_φ in the model. This can be related to the fact that our non self-consistent procedure is not particularly reliable in the very inner disk close to the bar region. It could also reveal that our constant pattern speed bar is not enough to explain the richness of the data within this plane (Chiba et al. 2021), that we are missing the effect of vertical perturbations (e.g. Laporte et al. 2019, 2020), as well as accreted
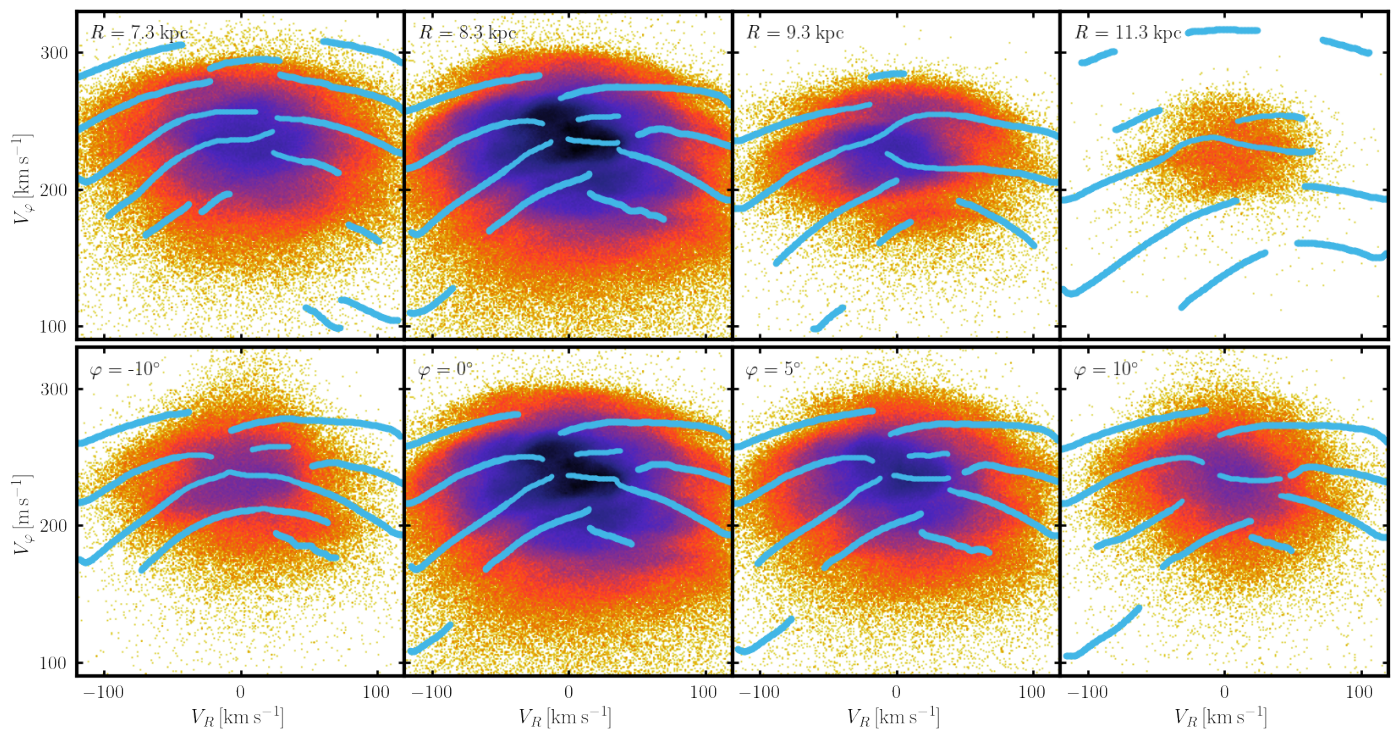
Fig. 10. 2-D histogram distribution of the Gaia RVS disk sample on the (V_R, V_φ) plane for stars within $|\varphi| < 2.4°$ and $|R - R_i| < 300$ pc at different radii $R_i \in [7.3, 8.3, 9.3, 11.3]$ kpc (top row), and for stars within $|R - R_0| < 300$ pc and $|\varphi - \varphi_j| < \arctan\left(\frac{300 \text{ pc}}{8275 \text{ pc}}\right)$ at different azimuthal angles $\varphi_j \in [-10°, 0°, 5°, 10°]$ (bottom row). The colored lines show the peaks identified in our *model* with the method of Bernet et al. (2022, 2024).

prograde structures, although all this would require further investigations.

5.4. Moving groups across the disk

In Bernet et al. (2022, 2024), a methodology was developed to perform a blind search for moving groups in Gaia data across the whole disk, based on the execution of a Wavelet Transform in independent small volumes of the disk followed by a grouping into global structures with the Breadth-first search algorithm from Graph Theory. Fixing a given V_R, one can then for instance look at the evolution of the location of moving groups in the (R, V_φ) plane at the azimuth of the Sun, or in the (φ, V_φ) plane at the radius of the Sun. In Fig. 9, we overlay the structures found in Gaia DR3 on top of the density from our model. The azimuthal distribution of moving groups (right panels of Fig. 9) is well in line with the slopes from our model at the Solar radius, while the radial distribution at the Solar azimuth (left panels of Fig. 9) also appears globally in line with the data apart from the low $V_\varphi \leq 200$ kms^{-1} region for small $R \leq 6.5$ kpc (the ridges of the model having a much too high slope in that region of phase-space), where the bar self-gravity is probably having a non-negligible effect on the data.

Interestingly, in the model, the Hercules moving group at the Solar radius appears to result from the merging of two ridges at smaller radii, seen as dark regions on Fig. 9 in the underlying density of the model, one with a slope compatible with the observed radial gradient of the Hercules moving group, essentially caused by the bar, and another one with a larger slope, mostly due to spiral arms. This is especially clear at positive V_R, where the two ridges are clearly separated at $R < 7$ kpc in the model, while this separation appears to leave a similar signature within

the data too. At $V_R = 0$, the split can also be seen, although it also merges with the inner continuation of the Hyades moving group. At negative V_R, the agreement is less good, though in the region where Hercules is expected to dominate less: the second ridge of Hercules overlaps with the Hyades ridge at $R \sim 7$ kpc in the model, whilst in the data this is only seen as a small upward bend in the Hyades ridge, corresponding to the merging of the ridges in the model. This second Hercules ridge is clearly an effect of spiral arms, while the major Hercules one is produced by the bar alone. The joint effect of the multiple bar modes in the present model, together with the axisymmetric background potential used, might explain the differences with Bernet et al. (2024).

Conversely, we apply the method of Bernet et al. (2022, 2024) on the *model* and overlay on Fig. 10 the detected groups on top of Gaia data at different radii at the azimuth of the Sun, and at different azimuths at the Solar radius. Visually, some features are stikingly similar in the model and data. An interesting point to note is that, even though not clearly visible by eye, the model does seem to recover an overdensity at the Sun's position (bottom-right feature in the second panels from the left on Fig. 10) that can be identified with the location of the Bobylev/Hercules-2 bimodality of Hercules, although much less strongly than in the data.

5.5. Orbit of the Sun

As an example of application of our model, we propose to compare the orbit of the Sun in the background axisymmetric model to that in our fiducial non-axisymmetric one. The result is displayed on Fig. 11. In the axisymmetric case, the radial period is 161.5 Myr, and the Sun is now close to reaching its peri-

center. The time between the last pericentric passage and the one that we are about to reach is a bit smaller in the non-axisymmetric model, namely 154.5 Myr. The previous pericentric passage, which happened a bit later in the non-axisymmetric model, was also closer to the Galactic center than in the axisymmetric case. The last apocenter was very similar in both models, but the next-to last one was further away in the outer Galaxy in the non-axisymmetric case, for which radial amplitudes are typically larger. If we look at the evolution of the surface density at the Sun's position with time, the picture becomes more complicated. The time between the last surface density maximum and the one that we are about to reach (i.e., still 161.5 Myr in the axisymmetric case) is a bit larger in the non-axisymmetric case, namely 185 Myr, because we will be temporarily following the Local arm overdensity on our journey back to the outer disk. Also, when looking back at $t \sim -250$ Myr, the apocenter that corresponds to a minimum in the surface density of the axisymmetric model does actually correspond to a local maximum in the non-axisymmetric case, because the Sun was also following a spiral arm at that time. This could have interesting consequences in studying cyclic sedimentation on Earth on long timescales (e.g., Boulila et al. 2018). Since spiral arms are generally expected to arise from a recurrent cycle of groove or edge modes, it is however impossible to trace back the Sun's orbit on longer timescales than a few 100 Myr, at least without resorting to detailed chemodynamical modelling of the evolution of the whole Galactic disk.
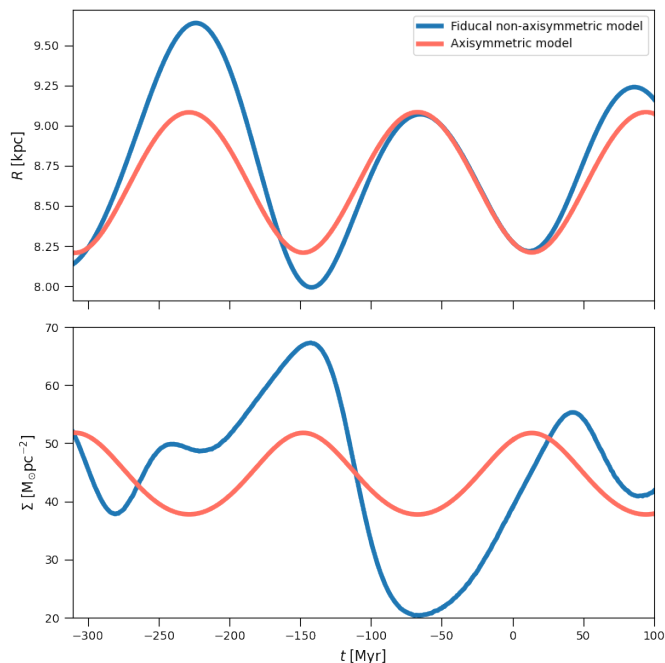
Fig. 11. Top panel: Galactocentric radius of the Sun as a function of time in the background axisymmetric (orange) and fiducial non-axisymmetric (blue) models. Bottom panel: Evolution of the surface density at the Sun's position with time.

5.6. Orbits of young associations

Young ($\sim$ 50 Myr) stellar associations can typically be traced back to their original position by integrating their orbits backward in a given Galactic potential. To illustrate the importance of taking into account the non-axisymmetries of the potential for such a procedure, we integrate forward in time for 50 Myr four archetypical young stellar associations at different positions in the Galactic disk within our fiducial non-axisymmetric model. Each association is represented by 20 stars that are dispersed in velocity and space with Gaussians of standard deviation of 1 kms^{-1} in V_R and V_φ around the circular velocity, and of 2 pc around the positions (x, y) = (10.6 kpc, -2.4 kpc), (8.7 kpc, -0.3 kpc), (7.1 kpc, 0.4 kpc), (6.0 kpc, -0.5 kpc). We then integrate them backward in time both in the fiducial non-axisymmetric model and in the background axisymmetric model. The associations typically go back to a position that can be erroneous by more than 150 pc in the axisymmetric case, with an elongated shape very different from the true orginal configuration.
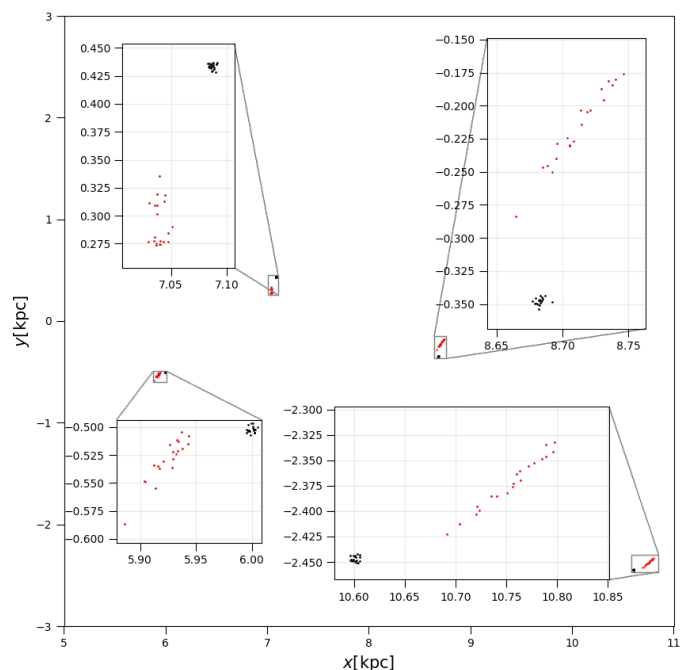

Fig. 12. The implication of the non-axisymmetries on the orbits of young associations is illustrated by integrating four young associations for 50 Myr forward in the fiducial potential and then backward in time with both the erroneous axisymmetric model (red) and the fiducial one (black). The insets show zoom-ins around the regions of the associations.

6. Discussion and conclusions

We used the in-plane velocities of a sample of disk stars with six-dimensional phase-space information from Gaia-StarHorse in order to fit a Galactic potential model that includes a detailed parametric shape for the bar and spiral arms, using the backward integration method. The adjusted observable quantities were the median Galactocentric radial velocity, for a selection of points within the Galactic plane, complemented by additional constraints from local velocity space at the Sun's position. All the parameters of the fiducial non-axisymmetric potential are summarized in Table 2, within the background axisymmetric potential fixed in Table 1. It is remarkable that such a purely dynamical fit recovers many of the known locations of spiral arm over-densities detected from photometry within the disk (Fig. 5). These spiral arms can be interpreted as groove or edge modes

such as those found in *N*-body simulations. In the Solar vicinity, we identify the Local arm as a strong gravitational perturbation, in accordance with independent probes of the local non-axisymmetric potential by Widmark & Naik (2024). We also recover the observed map of median radial actions in the extended Solar vicinity (Fig. 6), as well as a good qualitative agreement with the detailed variation with radius and azimuth of moving groups identified in Gaia data (Fig. 9). The latter is truly remarkable since the model was not directly fit to these phase-space features. The only (locally) fitted moving group was Sirius, entirely absent from the bar-only model: we note that it is nevertheless still characterized by a weaker peak in the fiducial model than in the data. While our best candidate model may well be a local minimum in parameter space, the latter being particularly vast, especially if letting the parameters of the background axisymmetric density and DF vary too, we nevertheless argue that it can, for the time being, be used as a fiducial non-axisymmetric potential for the Galaxy, for instance in order to confidently integrate in-plane orbits. The code to generate local velocity space distributions as well as radial velocity maps is made public.

This paper represents only a first quantitative step in the direction of establishing a detailed three-dimensional non-axisymmetric potential for the Milky Way. Future improvements of our present investigations will be to explore its three-dimensional consequences, first in forward test-particle integrations (see, e.g., Faure et al. 2014; Monari et al. 2016b), as both the bar (Thomas et al. 2023) and spiral (Cox & Gomez 2002) potentials can readily be generalized to three dimensions. Let us also note that we have made the assumption that the spiral arms cannot live inside the corotation resonance of the bar ($R = 6.6$ kpc in our fiducial model), an assumption that could potentially be partially lifted: we already checked that it does not affect much our best candidate model. However, a proper fit of these inner regions of the Galactic disk would require us to make the model self-consistent. The absence of self-consistency can become a serious issue in the innermost parts of the Galaxy, where the bar perturbation is itself the tracer. Some deficiencies of our model at low radii and low angular momenta have indeed already been identified in Fig. 8 and Fig. 9. Although beyond the scope of the present work, future improvements of our model might rely on an adaptation of the self-consistent made-to-measure method in order to account for self-consistency. One should also point out that the background model (axisymmetric potential and DF) have not themselves been fitted here, and could in principle also be adjusted to the data. This would increase the parameter space and might require us to use machine learning methods to efficiently explore the full parameter space. A parallel improvement will be to incorporate a detailed selection function in the fitting procedure (e.g., Castro-Ginard et al. 2023; Khanna et al. 2024), compute a proper posterior (and error bars) on the best-fit parameters, while perhaps attempting to separate the stellar populations into distinct DFs. Finally, when moving to three dimensions, it is obvious that vertical perturbations of the disk, e.g. from the Sagittarius dwarf, will have to be included too, together with a possible time-variation of the bar pattern speed.

In summary, the fiducial model presented here, reproducing a larger amount of observables than ever before, does represent a significant advance in our understanding of the non-axisymmetric structure of the Milky Way disk. However, it is important to recognize its limitations and to continue improving it in order to obtain an even more accurate representation of our Galaxy.

Code availability

The "Spiral and Bar Backward Integration" (SPIBACK) `PyTorch`-based code to generate local velocity space distributions as well as median radial velocity maps is publicly available at: `https://github.com/yrkhalil/SPIBACK`

References

Al Kazwini, H., Agobert, Q., Siebert, A., et al. 2022, A&A, 658, A50
Amaral, L. H. & Lepine, J. R. D. 1997, MNRAS, 286, 885
Anders, F., Khalatyan, A., Queiroz, A. B. A., et al. 2022, A&A, 658, A91
Antoja, T., Figueras, F., Fernández, D., & Torra, J. 2008, A&A, 490, 135
Antoja, T., Helmi, A., Bienayme, O., et al. 2012, MNRAS, 426, L1
Antoja, T., Helmi, A., Dehnen, W., et al. 2014, A&A, 563, A60
Antoja, T., Helmi, A., Romero-Gómez, M., et al. 2018, Nature, 561, 360
Astropy Collaboration, Price-Whelan, A. M., Lim, P. L., et al. 2022, apj, 935, 167
Baba, J., Saitoh, T. R., & Wada, K. 2013, ApJ, 763, 46
Benjamin, R. A., Churchwell, E., Babler, B. L., et al. 2005, ApJ, 630, L149
Bernet, M., Ramos, P., Antoja, T., et al. 2022, A&A, 667, A116
Bernet, M., Ramos, P., Antoja, T., Monari, G., & Famaey, B. 2024, A&A, 686, A92
Binney, J. 2010, MNRAS, 401, 2318
Binney, J. 2012, MNRAS, 426, 1324
Binney, J. 2020, MNRAS, 495, 895
Binney, J., Gerhard, O., & Spergel, D. 1997, MNRAS, 288, 365
Binney, J., Gerhard, O. E., Stark, A. A., Bally, J., & Uchida, K. I. 1991, MNRAS, 252, 210
Binney, J. & McMillan, P. 2011, Monthly Notices of the Royal Astronomical Society, 413, 1889–1898
Binney, J. & Schönrich, R. 2018, MNRAS, 481, 1501
Binney, J. & Tremaine, S. 2008, Galactic Dynamics: Second Edition (Princeton University Press)
Binney, J. & Vasiliev, E. 2023, MNRAS, 520, 1832
Bissantz, N., Englmaier, P., & Gerhard, O. 2003, MNRAS, 340, 949
Boulila, S., Laskar, J., Haq, B. U., Galbrun, B., & Hara, N. 2018, Global and Planetary Change, 165, 128
Callingham, T. M., Cautun, M., Deason, A. J., et al. 2019, MNRAS, 484, 5453
Castro-Ginard, A., Brown, A. G. A., Kostrzewa-Rutkowska, Z., et al. 2023, A&A, 677, A37
Castro-Ginard, A., McMillan, P. J., Luri, X., et al. 2021, A&A, 652, A162
Chen, R. T. Q. 2018, torchdiffeq
Chiba, R., Friske, J. K. S., & Schönrich, R. 2021, MNRAS, 500, 4710
Chiba, R. & Schönrich, R. 2021, MNRAS, 505, 2412
Churchwell, E., Babler, B. L., Meade, M. R., et al. 2009, PASP, 121, 213
Clarke, J. P., Wegg, C., Gerhard, O., et al. 2019, MNRAS, 489, 3519
Cox, D. P. & Gomez, G. C. 2002, The Astrophysical Journal Supplement Series, 142, 261–267

De Rijcke, S., Fouvry, J.-B., & Pichon, C. 2019, MNRAS, 484, 3198
De Rijcke, S. & Voulis, I. 2016, MNRAS, 456, 2024
de Salas, P. F. & Widmark, A. 2021, Reports on Progress in Physics, 84, 104901
de Vaucouleurs, G. 1964, in The Galaxy and the Magellanic Clouds, ed. F. J. Kerr, Vol. 20, 195
Debattista, V. P., Gerhard, O., & Sevenster, M. N. 2002, MNRAS, 334, 355
Debattista, V. P., Khachaturyants, T., Amarante, J. A. S., et al. 2024, arXiv e-prints, arXiv:2402.08356
Dehnen, W. 1998, AJ, 115, 2384
Dehnen, W. 1999a, AJ, 118, 1190
Dehnen, W. 1999b, ApJ, 524, L35
Dehnen, W. 2000, AJ, 119, 800
Dillamore, A. M., Belokurov, V., & Evans, N. W. 2024, MNRAS, 532, 4389
D'Onghia, E. & Aguerri, J. A. L. 2020, ApJ, 890, 117
Drimmel, R. 2000, A&A, 358, L13
Drimmel, R. & Spergel, D. N. 2001, ApJ, 556, 181
Eilers, A.-C., Hogg, D. W., Rix, H.-W., et al. 2020, ApJ, 900, 186
Englmaier, P. & Gerhard, O. 1999, MNRAS, 304, 512
Famaey, B. & Dejonghe, H. 2003, MNRAS, 340, 752
Famaey, B., Jorissen, A., Luri, X., et al. 2005, A&A, 430, 165
Famaey, B., Pont, F., Luri, X., et al. 2007, A&A, 461, 957
Famaey, B., Siebert, A., & Jorissen, A. 2008, A&A, 483, 453
Faure, C., Siebert, A., & Famaey, B. 2014, MNRAS, 440, 2564
Fiteni, K., De Rijcke, S., Debattista, V. P., & Caruana, J. 2024, MNRAS, 529, 4879
Fragkoudi, F., Katz, D., Trick, W., et al. 2019, MNRAS, 488, 3324
Frankel, N., Hogg, D. W., Tremaine, S., Price-Whelan, A., & Shen, J. 2024, arXiv e-prints, arXiv:2407.07149
Friske, J. K. S. & Schönrich, R. 2019, MNRAS, 490, 5414
Fux, R. 1999, A&A, 345, 787
Fux, R. 2001, A&A, 373, 511
Gaia Collaboration, A. Vallenari, Brown, A. G. A., et al. 2023a, A&A, 674, A1
Gaia Collaboration, Brown, A. G. A., Vallenari, A., et al. 2018a, A&A, 616, A1
Gaia Collaboration, Brown, A. G. A., Vallenari, A., et al. 2021, A&A, 649, A1
Gaia Collaboration, Drimmel, R., Romero-Gómez, M., et al. 2023b, A&A, 674, A37
Gaia Collaboration, Katz, D., Antoja, T., et al. 2018b, A&A, 616, A11
Georgelin, Y. M. & Georgelin, Y. P. 1976, A&A, 49, 57
Gerhard, O. E. & Vietri, M. 1986, MNRAS, 223, 377
Hamilton, C. 2024, MNRAS, 528, 5286
Hamilton, C., Tolman, E. A., Arzamasskiy, L., & Duarte, V. N. 2023, ApJ, 954, 12
Haywood, M., Khoperskov, S., Cerqui, V., et al. 2024, A&A, 690, A147
Hilmi, T., Minchev, I., Buck, T., et al. 2020, MNRAS, 497, 933
Horta, D., Petersen, M. S., & Peñarrubia, J. 2024, arXiv e-prints, arXiv:2402.07986
Hou, L. G., Han, J. L., & Shi, W. B. 2009, A&A, 499, 473
Hunt, J. A. S. & Bovy, J. 2018, MNRAS, 477, 3945
Hunt, J. A. S., Bub, M. W., Bovy, J., et al. 2019, MNRAS, 490, 1026
Hunt, J. A. S., Hong, J., Bovy, J., Kawata, D., & Grand, R. J. J. 2018, MNRAS, 481, 3794
Ibata, R., Malhan, K., Tenachi, W., et al. 2024, ApJ, 967, 89
Jiao, Y., Hammer, F., Wang, H., et al. 2023, A&A, 678, A208
Khanna, S., Yu, J., Drimmel, R., et al. 2024, arXiv e-prints, arXiv:2410.22036
Laporte, C. F. P., Famaey, B., Monari, G., et al. 2020, A&A, 643, L3
Laporte, C. F. P., Minchev, I., Johnston, K. V., & Gómez, F. A. 2019, MNRAS, 485, 3134
Levine, E. S., Blitz, L., & Heiles, C. 2006, Science, 312, 1773
Li, C., Siebert, A., Monari, G., Famaey, B., & Rozier, S. 2023, MNRAS, 524, 6331
Li, C., Yuan, Z., Monari, G., et al. 2024, A&A, 690, A26
Li, Z., Gerhard, O., Shen, J., Portail, M., & Wegg, C. 2016, ApJ, 824, 13
Lin, C. C. & Shu, F. H. 1964, ApJ, 140, 646
Lin, C. C., Yuan, C., & Shu, F. H. 1969, ApJ, 155, 721
Lucchini, S., D'Onghia, E., & Aguerri, J. A. L. 2024, MNRAS, 531, L14
Lynden-Bell, D. & Kalnajs, A. J. 1972, MNRAS, 157, 1
Malhan, K. & Ibata, R. A. 2019, MNRAS, 486, 2995
Minchev, I., Nordhaus, J., & Quillen, A. C. 2007, ApJ, 664, L31
Monari, G., Famaey, B., Carrillo, I., et al. 2018, A&A, 616, L9
Monari, G., Famaey, B., Fouvry, J.-B., & Binney, J. 2017, MNRAS, 471, 4314
Monari, G., Famaey, B., & Siebert, A. 2016a, MNRAS, 457, 2569
Monari, G., Famaey, B., Siebert, A., et al. 2019a, A&A, 632, A107
Monari, G., Famaey, B., Siebert, A., et al. 2016b, MNRAS, 461, 3835
Monari, G., Famaey, B., Siebert, A., Wegg, C., & Gerhard, O. 2019b, A&A, 626, A41
Monari, G., Helmi, A., Antoja, T., & Steinmetz, M. 2014, A&A, 569, A69
Morgan, W. W., Sharpless, S., & Osterbrock, D. 1952, AJ, 57, 3
Oort, J. H., Kerr, F. J., & Westerhout, G. 1958, MNRAS, 118, 379
Ou, X., Eilers, A.-C., Necib, L., & Frebel, A. 2024, MNRAS, 528, 693
Palicio, P. A., Recio-Blanco, A., Poggio, E., et al. 2023, A&A, 670, L7

Paszke, A., Gross, S., Massa, F., et al. 2019, in Advances in Neural Information Processing Systems 32 (Curran Associates, Inc.), 8024–8035
Pérez-Villegas, A., Portail, M., Wegg, C., & Gerhard, O. 2017, ApJ, 840, L2
Peters, W. L., I. 1975, ApJ, 195, 617
Poggio, E., Drimmel, R., Cantat-Gaudin, T., et al. 2021, A&A, 651, A104
Pompéia, L., Masseron, T., Famaey, B., et al. 2011, MNRAS, 415, 1138
Portail, M., Gerhard, O., Wegg, C., & Ness, M. 2017, MNRAS, 465, 1621
Quillen, A. C., Dougherty, J., Bagley, M. B., Minchev, I., & Comparetta, J. 2011, MNRAS, 417, 762
Ramos, P., Antoja, T., & Figueras, F. 2018, A&A, 619, A72
Reid, M. J., Menten, K. M., Brunthaler, A., et al. 2019, ApJ, 885, 131
Roche, C., Necib, L., Lin, T., Ou, X., & Nguyen, T. 2024, ApJ, 972, 70
Sanders, J. L. & Binney, J. 2016, MNRAS, 457, 2107
Sanders, J. L., Smith, L., & Evans, N. W. 2019, MNRAS, 488, 4552
Sellwood, J. A. 1993, in American Institute of Physics Conference Series, Vol. 278, Back to the Galaxy, ed. S. S. Holt & F. Verter, 133–136
Sellwood, J. A. & Carlberg, R. G. 2014, ApJ, 785, 137
Sellwood, J. A. & Carlberg, R. G. 2019, MNRAS, 489, 116
Sellwood, J. A. & Masters, K. L. 2022, ARA&A, 60 [arXiv:2110.05615]
Shen, J. & Zheng, X.-W. 2020, Research in Astron. and Astrophys., 20, 159
Siebert, A., Famaey, B., Binney, J., et al. 2012, MNRAS, 425, 2335
Sormani, M. C., Binney, J., & Magorrian, J. 2015, MNRAS, 454, 1818
Storn, R. & Price, K. 1997, Journal of Global Optimization, 11, 341
Syer, D. & Tremaine, S. 1996, MNRAS, 282, 223
Thomas, G. F., Famaey, B., Monari, G., et al. 2023, A&A, 678, A180
Tremaine, S., Frankel, N., & Bovy, J. 2023, MNRAS, 521, 114
Tremaine, S. & Weinberg, M. D. 1984, ApJ, 282, L5
Trick, W. H. 2022, MNRAS, 509, 844
Trick, W. H., Coronado, J., & Rix, H.-W. 2019, MNRAS, 484, 3291
Trick, W. H., Fragkoudi, F., Hunt, J. A. S., Mackereth, J. T., & White, S. D. M. 2021, MNRAS, 500, 2645
Urquhart, J. S., Figura, C. C., Moore, T. J. T., et al. 2014, MNRAS, 437, 1791
Vasiliev, E. 2018, AGAMA: Action-based galaxy modeling framework, Astrophysics Source Code Library, record ascl:1805.008
Vasiliev, E. 2019, MNRAS, 482, 1525
Vauterin, P. & Dejonghe, H. 1997, MNRAS, 286, 812
Vázquez, R. A., May, J., Carraro, G., et al. 2008, ApJ, 672, 930
Virtanen, P., Gommers, R., Oliphant, T. E., et al. 2020, Nature Methods, 17, 261
Vislosky, E., Minchev, I., Khoperskov, S., et al. 2024, MNRAS, 528, 3576
Wegg, C., Gerhard, O., & Portail, M. 2015, MNRAS, 450, 4050
Weiland, J. L., Arendt, R. G., Berriman, G. B., et al. 1994, ApJ, 425, L81
Widmark, A. & Monari, G. 2019, MNRAS, 482, 262
Widmark, A. & Naik, A. P. 2024, A&A, 686, A70
Xu, Y., Hou, L. G., Bian, S. B., et al. 2021, A&A, 645, L8
Yuan, Z., Li, C., Martin, N. F., et al. 2024, A&A, 691, L1
Zhao, H., Spergel, D. N., & Rich, R. M. 1994, AJ, 108, 2154

Appendix A: A simple formula for approximately locating bar resonances in velocity space

In order to evaluate analytically the location of the phase-space resonant zones due to a constant pattern speed bar perturbation, one should define those zones in terms of librating versus circulating orbits after canonically transforming to slow and fast action and angle variables (e.g. Monari et al. 2017; Binney 2020). This is a relatively arduous task, and we propose here a less precise but much faster way to roughly estimate the location of resonant ridges in local velocity space, or more accurately the surfaces of phase-space where the resonant condition is fulfilled. This simple formula will be, by construction, axisymmetric, which means that one cannot use it to model the changes in the morphology of the resonant surfaces with azimuth. The formula relies on locally drawing constant energy lines in the V_R-V_φ plane within the improved epicyclic formalism presented in Dehnen (1999a). For convenience, we reproduce here their equations 28 and 29 for the radial evolution of an orbit:

$$R(\eta) = R_E \left[1 - e \cos(\eta)\right]^{\frac{\gamma}{2}}, \tag{A.1}$$

$$e = \sqrt{1 - \left(\frac{J_\varphi}{J_\varphi^{\text{circ}}}\right)^2}, \tag{A.2}$$

where J_φ^{circ} and R_E are, respectively, the angular momentum and radius of a circular orbit of the same energy, $\gamma = \gamma(R_E) = 2\Omega(R_E)/\kappa(R_E)$ is the ratio of the circular frequency Ω over the radial epicyclic frequency κ as usual, and e is the eccentricity of the orbit. The phase in radius evolving with time t, namely $\eta(t)$, is the parameter that represents the position along the path of the orbit, and is defined as a function of the eccentricity and the radial epicyclic frequency (see Eq. 28d of Dehnen 1999a). For simplicity, we consider that $\eta \sim \kappa t$, which in turn means that the radial velocity can be calculated as:

$$V_R = \frac{dR}{d\eta}\frac{d\eta}{dt} \sim \kappa \frac{\gamma}{2} R(\eta) \frac{e \sin(\eta)}{1 - e \cos(\eta)} = V_c(R_E) \frac{R}{R_E} \frac{e \sin(\eta)}{1 - e \cos(\eta)}. \tag{A.3}$$

The azimuthal velocity, on the other hand, can be written as a function of R simply by the conservation of angular momentum: $V_\varphi = J_\varphi/R(\eta)$. Using Eq. A.1 and Eq. A.2 , one then gets a closed form equation that relates the changes of V_R along the orbit to those of R, V_φ and the circular velocity curve:

$$V_R = V_c(R_E) \left(\frac{R}{R_E}\right)^{\frac{\gamma-2}{\gamma}} \sqrt{2\left(\frac{R}{R_E}\right)^{\frac{2}{\gamma}} - \left(\frac{R}{R_E}\right)^{\frac{4}{\gamma}} - \left(\frac{R V_\varphi}{J_\varphi^{\text{circ}}}\right)^2}. \tag{A.4}$$

All that is left is to impose the constraint that stars be on a surface where the resonant condition is met. Under the assumption that frequencies are functions solely of the energy, the resonant condition is preserved as long as stars share the same J_φ^{circ} and R_E, and as longs as these are equal to the radius and angular momentum where the circular orbit is $l : m$ resonant. We refer to these as R_{res}, such that $l \kappa(R_{\text{res}}) + m [\Omega(R_{\text{res}}) - \Omega_b] = 0$, and as $J_\varphi^{\text{res}} \equiv R_{\text{res}} V_c(R_{\text{res}})$, respectively. The final equation for the surfaces of resonant condition is then:

$$V_\varphi^{\text{res}}(R, V_R) = \frac{J_\varphi^{\text{res}}}{R} \sqrt{2\left(\frac{R}{R_{\text{res}}}\right)^{\frac{2}{\gamma}} - \left(\frac{R}{R_{\text{res}}}\right)^{\frac{4}{\gamma}} \left[1 + \left(\frac{R_{\text{res}}}{R} \frac{V_R}{V_c(R_{\text{res}})}\right)^2\right]}. \tag{A.5}$$

where we reordered the terms to express V_φ as a function of the other phase-space variables.

The application of Eq. A.5 to the V_R-V_φ velocity plane produces for each resonance a curve that is almost identical to Eq. 9 from Dehnen (2000), and is equivalent to drawing lines of constant energy at a given configuration space point, because it is written under the assumption that the orbital frequencies are pure functions of the orbital energy. As can be seen on Fig. A.1, in our best bar model, this formula identifies extremely well the peak of the overdensities produced at $R = R_0$ by the $6 : 1$, $4 : 1$ and $2 : 1$ outer resonances of the bar. For the $(l, m) = (0, 2)$ corotation resonance, the formula fails, probably because the eccentricty becomes too large, and it rather approximately identifies the lower bound of the resonant zone.
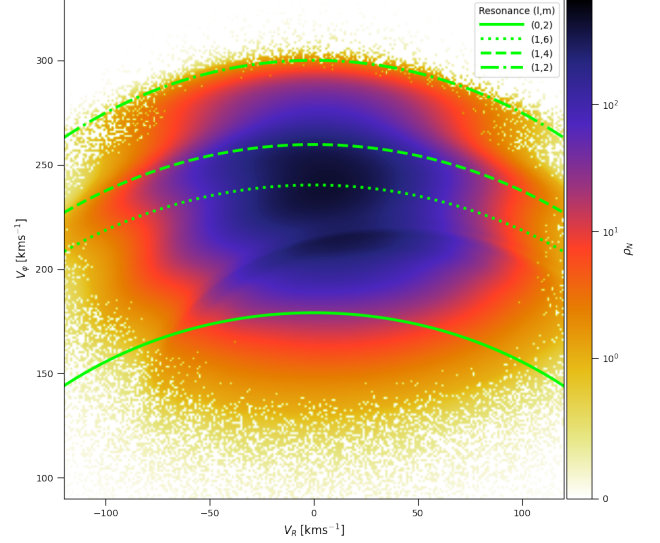

Fig. A.1. Resonant lines V_φ^{res} as a function of V_R from Eq. A.5 at $R = R_0$, computed with the potential of Table 1, for a bar pattern speed of $37 \text{ km s}^{-1} \text{ kpc}^{-1}$. The lines are overlaid on top of the local velocity space density produced by our preferred bar-only model at the Sun's position.